Long-Term Intestinal Epithelial Remodeling Induced by Acute Protein-Energy Malnutrition

Fenja A. Schuran[1,*], Neha Mishra[1,*], Víctor A. López-Agudelo[1], Nina Sommer[1], Joana P. Bernardes[1], Alesia Walker[2], Finn Hinrichsen[1,3], Ting Gong[1], Felix Gilbert[1,3], Lena Schröder[1], Archana Bhardwaj[1], Sven Künzel[4], Saskia Weber-Stiehl[1], Go Ito[5], Florian Tran[1,3], Matthieu Groussin[1,6], Christoph Röcken[7], Juan Matute[,8,9], Stefan Schreiber[3], Josef M. Penninger[10,11,12], Richard S. Blumberg[8], Philippe Schmitt-Kopplin[2], John F. Baines[4,13], Felix Sommer[1,#] & Philip Rosenstiel[1,3#]

[1] Institute of Clinical Molecular Biology, University of Kiel and University Hospital Schleswig-Holstein, Rosalind-Franklin-Straße 12, 24105 Kiel, Germany

[2] Research Unit Analytical BioGeoChemistry, Helmholtz Zentrum München, German Research Center for Environmental Health, Ingolstädter Landstrasse 1, 85764 Neuherberg, Germany.

[3] Dep. of Internal Medicine I, University Hospital Schleswig-Holstein, Campus Kiel, Arnold-Heller-Straße 3, 24105 Kiel, Germany

[4] Max-Planck-Institute for Evolutionary Biology, August-Thienemann-Straße 2, 24306 Plön, Germany

[5] Department of Gastroenterology and Hepatology, Institute of Science Tokyo, 2 Chome-12-1 Ookayama, 152-8550, Tokyo, Japan

[6]The Global Microbiome Conservancy, Massachusetts Institute of Technology, Cambridge, Massachusetts, USA.

[7]Department of Pathology, Christian-Albrechts-University, University Hospital Schleswig-Holstein, 24105, Kiel, Germany.

[8]Gastroenterology Division, Department of Medicine, Brigham and Women's Hospital, Harvard Medical School, 77 Avenue Louis Pasteur, Boston MA 02115, USA

[9]current address: Division of Neonatology, Department of Pediatrics, Children's Hospital of Philadelphia, Perelman School of Medicine at the University of Pennsylvania, 3401 Civic Center Blvd, Philadelphia PA 19004, USA

[10]Department of Laboratory Medicine, Medical University of Vienna, Währinger Gürtel 18-20, 1090 Vienna, Austria

[11] Helmholtz Centre for Infection Research, Inhoffenstraße 7, 38124 Braunschweig, Germany

[12]Department of Medical Genetics, Life Sciences Institute, University of British Columbia, Vancouver V6T 1Z3, Canada

[13]Institute of Experimental Medicine, University of Kiel, Michaelisstr. 5, 24105 Kiel, Germany

[*] Authors contributed equally with shared first authorship.

[#] Shared senior authorship.

Keywords: Protein energy malnutrition / intestinal inflammation/ Paneth cell / microbiome / GDF15 / intestinal epithelium

Correspondence:

Philip Rosenstiel (p.rosenstiel@mucosa.de) and Felix Sommer (f.sommer@ikmb.uni-kiel.de)

Abstract

Protein-energy malnutrition (PEM) is a global health burden with lasting effects that extend well beyond the initial nutrient deficiency. To systematically investigate the long-term effects of a single episode of PEM on the structure and function of the intestinal epithelium and its associated microbiota, we employed a comprehensive multi-omics approach, including (spatial) transcriptomics, DNA methylation analysis, fecal metagenomics, and metabolomics. Our findings show that PEM persistently alters the intestinal epithelium by depleting Paneth cells and suppressing antimicrobial gene expression - changes linked to DNA methylation that persist despite dietary recovery. In germ-free mice, the sustained epithelial phenotype after was absent. We identified the microbial lipid metabolite 9-HODE and epigenetically deregulated PPAR-driven GDF15 expression as key molecular drivers of the persistent PEM-induced Paneth cell dysfunction. Targeting microbial lipid production and its link to the host GDF15 pathway could offer novel therapeutic strategies for long-term consequences of malnutrition and other Paneth cell-associated diseases.

59 **Introduction**

60 Undernutrition is a major global health burden and is responsible for 45% of child deaths
61 world-wide [1,2]. It is defined as a disordered nutritional state resulting from a combination of
62 inflammation and a negative nutrient balance, leading to changes in body composition,
63 function and outcome and associated disorders [3]. Clinically, undernutrition has several facets,
64 ranging from a mild caloric and/or micronutrient deficit to more severe forms resulting from
65 sustained inadequate uptake of protein (protein energy malnutrition, termed PEM hereafter).
66 The latter is the main form of global undernutrition and combines an energy deficit with lack
67 of essential amino acids, which are necessary building blocks for new proteins and regulate
68 cellular energy homeostasis. PEM is by far the most important causative factor of morbidity
69 and mortality in developing countries and crisis regions, but also in industrialized countries
70 the growing socioeconomic gap and specifically increasing poverty at young and old age, are
71 linked to a significant burden of this disease state [4]. The gut microbiota has been convincingly
72 shown to be involved in the etiology of PEM [5–8] and microbiota-directed nutritional
73 interventions have been utilized to overcome acute periods of malnutrition [9–12].

74 Whereas the pathophysiology of acute PEM has been intensely studied [7], long-term
75 consequences of PEM and the molecular factors that contribute to such effects are not
76 sufficiently understood. These consequences are characterized by a "memory effect" on
77 specific body functions, which can be established after just one episode of malnutrition and
78 may even be inherited by future generations[13]. Malnutrition during fetal development or
79 early life can lead to ongoing poor weight gain and growth (known as stunting), which often
80 persists even when a normal diet is introduced during childhood. Other clinical features
81 associated with previous episodes of PEM include delayed motor [14] and intellectual
82 development [15–17] and predisposition to obesity [18] and Type 2 diabetes in adulthood [19–21].
83 Importantly, individuals who suffered from chronic malnutrition in the past are also more
84 vulnerable to intestinal infections and have a higher mortality rate due to infection-related
85 complications [22,23]. Previous PEM may extend the duration of infectious diarrhea [24],
86 potentially due to a decrease of intestinal barrier function, facilitating translocation of
87 commensal bacteria and pathogens. We had previously shown that a lack of ACE2/BOAT1-
88 dependent absorption of tryptophan in intestinal epithelial cells of mice may be a pivotal link
89 between malnutrition, commensal bacteria and intestinal inflammation [25], but the duration

90 and the exact cellular mechanism of this effect remained unclear. Early studies have shown
91 that PEM may sustainably hinder the growth of epithelial cells in the small intestinal crypts,
92 causing delayed cellular migration along the crypt-villus axis [26]. This may result in a delay in
93 the restoration of the epithelial structure and the recovery of the enzymatic and absorptive
94 capacity in malnourished individuals [27]. Moreover, serum anti-antibodies to intestinal
95 microbial antigens (e.g. flagellin, LPS) are persistently elevated after PEM, indicating an
96 insufficient barrier function and sustained immune responses against the gut microbiota [28–
97 30]. Despite this wealth of observations pointing towards fundamental long-term effects of
98 PEM on the intestinal mucosa, the effector mechanisms, e.g. microbe-derived metabolites
99 acting on cell fate decisions, remains largely unexplained. Here, we employed a murine model
100 of adult PEM to systematically understand long-term effects of severe episode of protein
101 undernutrition on the structure and functionality of the intestinal mucosa and its associated
102 microbiota.

Results

Persistent consequences of experimental protein energy malnutrition in the small intestine of adult mice.

Protein-restricted isocaloric diets in mice have been suggested to resemble the acute phenotype of protein energy malnutrition [23,31,33]. To establish a dietary PEM model in mice, we first conducted a pilot study to assess the ability of isocaloric experimental diets with different protein levels (0.7%, 2%, 5% protein, hereafter termed “PEM diet”) to cause a PEM phenotype, as determined by the maximum weight loss within a four-week treatment period, compared to a standard diet with 20% protein, which is termed “control or ctrl diet” hereafter (Fig S1A). To investigate the long-term physiological effects of an episode of protein-energy malnutrition (PEM) on the intestinal tract, we conducted a dietary study using 10-week-old adult male C57 BL/6J mice. The mice were first subjected to a 4-week isocaloric PEM diet containing 0.7% protein, followed by a 6-week recovery phase on a regular control diet with 20% protein. (Figure 1A). After 4 weeks of 0.7% protein diet, mice lost approx. 25% of body weight compared to their littermates fed with control diet. After switching the recovery group to the control diet following 4 weeks of PEM, the mice experienced rapid weight gain during the first 2 weeks. However, by the end of the 6-week follow-up period, they had not fully regained the weight levels of the mice that had been maintained on the control diet for the entire duration of the study. Notably, this weight difference emerged after the mice had completed their axial growth, suggesting a lasting, "memory-like" effect of the prior PEM period in adult mice (Figure 1B). In a separate experiment, we confirmed that the dietary regimen successfully induced stunting in 4-week-old mice. However, we opted to proceed with the adult model to avoid potential secondary effects of perturbed developmental processes (Figure S2). No significant difference in food consumption was detected between the study groups (Figure 1C). As expected, PEM induced transient effects in several organ systems. We noticed decreased liver, epididymal white adipose tissue (EWAT) and spleen weight after 4 weeks of PEM diet (Figure S1B), which were however completely restored to the levels of their littermate controls after the shift to the control diet. Strikingly, exposure to PEM also led to several persistent changes in the intestinal tract. We observed a significantly reduced length of the small intestine in acute PEM and after recovery. While only subtle changes of crypt-villous architecture (crypt depth and villous length) were detectable (Figure

134 S1C), persistently reduced Ki-67 and TUNEL-positive epithelial cells indicated a slower
135 proliferation and turnover of the small intestinal epithelial lining as sequelae of PEM as shown
136 previously in humans [26,27]. This effect was limited to the small intestine, the primary site for
137 protein digestion and absorption. In contrast, the colon showed reduced length (Figure 1D)
138 and impaired epithelial proliferation (data not shown) only during the acute phase of PEM,
139 both of which fully normalized after 6 weeks on the control diet.
140

141 **Acute PEM induces a complex transcriptional dysregulation and leads to sustained**
142 **downregulation of anti-microbial defense modules in intestinal epithelial cells**

143 We next aimed to delineate the dynamics of the transcriptional response of intestinal
144 epithelial cells during PEM and after recovery. We performed RNA sequencing of purified
145 intestinal epithelial cells from the small intestine at acute PEM (4 weeks) and after 6 weeks
146 recovery (10 weeks). Principal component (PC) analysis showed a strong separation between
147 the acute PEM samples and all other conditions on the first PC (Figure S3A) indicating a severe
148 alteration of global transcriptome signatures of the epithelium under acute PEM. A total of
149 8,197 genes were differentially expressed as a result of PEM, with 4,190 downregulated and
150 4,007 upregulated, either during the acute phase or after recovery, compared to controls.
151 4,125 of these differentially expressed genes (DEGs) were unique to the acute PEM phase
152 only (2,007 down- and 2,118 upregulated genes). The upregulated PEM-specific DEGs
153 included genes involved in key metabolic processes, such as acyl-CoA dehydrogenases (Acadl,
154 Acadm, Acadvl, Acads, Acad11), phosphokinases (Khk, Tkfc), and glutathione transferases
155 (Gsta1, Gsta2, Gsta3, Gsta4, Gstm1, Gstm2, Gstm3, Gstm4, Gstm6, Gstp1, Gstp2, etc.). Gene
156 set enrichment analyses identified an over-representation of metabolic processes, including
157 beta-oxidation, glyceraldehyde-3-phosphate metabolism, and glutathione homeostasis, likely
158 reflecting a significant metabolic shift and heightened oxidative stress in response to PEM.
159 (Figures 2A, S3D). Among the downregulated DEGs, changes comprised decreased innate
160 immune and TNF production, such as *Cd14*, *Cd2*, *Ccr2*, *Ccr5*, *Ccr7*, *Il17a*, *Stat3*, *Tlr2* among
161 others (Figures 2A, S3D).

162 Following recovery, 3,791 genes were uniquely differentially expressed in post-PEM animals
163 compared to age-matched controls, with 2,011 genes downregulated and 1,781 upregulated.
164 (Figure S3B). Several DEGs followed an inverse pattern at acute PEM (4w) and recovery (10w)

165 suggesting compensatory regulatory processes after recovery from a period of protein
166 restriction, e.g. downregulation of fatty acid beta-oxidation and glutathione metabolism-
167 related DEGs relative to age-matched controls in gene set enrichment analyses (Figure S3D).

168 A comparison of the two timepoints to identify potential transcriptional "PEM-memory"
169 effects revealed an overlap of 281 DEGs (172 downregulated and 109 upregulated; Figure 2
170 and S3B). These genes exhibited consistent transcriptional regulation in the same direction
171 during both the acute phase of PEM (4 weeks) and after recovery (10 weeks), compared to
172 age-matched controls. Upregulated shared DEGs were enriched for differentiation-related
173 transcripts including *Dvl1* and *Dvl3* (Dishevelled Segment Polarity Protein 1 and 3), *Notch1*
174 (Neurogenic locus notch homolog protein 1), *Neurod1* (Neuronal Differentiation 1), which
175 pointed towards sustained alteration of epithelial lineage decisions (Figure 2B). Persistently
176 downregulated DEGs comprised a large body of antimicrobial effector molecules such as
177 several alpha-defensins (*Defa3, 17, 21, 22, 24, 26*), epithelial lysozyme (*Lyz1*) and intelectin
178 (*Itln1*), indicating an ongoing reduction of epithelial defense mechanisms after PEM (Figure
179 2D). To further explore the topographical distribution of epithelial alterations, we performed
180 spatial transcriptomics on intestinal tissues isolated from mice under acute PEM (4 weeks)
181 and age-matched controls (Figure 3C). Spots containing greater than 60% epithelial tissue
182 within the capture zone were manually selected and classified according to their anatomical
183 position, namely “Crypt”, “Villus-Intermediate” (including both bottom and middle sections)
184 and “Villus-Tip”, using high-resolution images of H&E-stained intestinal Swiss roles (Figure 3C,
185 S3F). When comparing these regions between control and PEM mice, we found that the
186 upregulated metabolic processes in PEM were primarily localized to the villi (Figure 3D),
187 whereas downregulation of antimicrobial effector molecules (*Defa3, 5, 17, 23, 26*) was
188 confined to the crypt region (Figure 3E).

189 As many of the genes involved in the transcriptional memory effect of PEM, such as Defa3,
190 Defa17, Defa21, Defa22, Defa24, Defa26, as well as Ang4, Hspb8, Itln1, and Lyz1 (Figure 2D,
191 3A), are recognized as Paneth cell marker genes, we next enumerated small intestinal Paneth
192 cells by lysozyme immunohistochemistry. Indeed, numbers of lysozyme-positive Paneth cells
193 were significantly reduced in the acute phase of PEM and remained at a much lower level
194 after recovery (Figure 3B). Proportions of Goblet cells, another cell type of the secretory
195 lineage, were unaffected (Figure S3C).

196 To test the long-term stability of PEM-dependent gene signatures, we isolated intestinal
197 organoids from mice during the PEM-recovery diet experiment at acute PEM (4 weeks) and
198 after recovery (10 weeks) including from CTRL diet-fed mice. These organoids were cultured
199 for at least five passages in regular organoid medium (no nutritional restriction), before RNA
200 was isolated and subjected to RNA sequencing. Comparing the general expression patterns
201 between intestinal epithelial cells isolated directly from the mice and cultured organoids
202 revealed a largely similar expression pattern both under acute PEM (Figure 4A) and after
203 recovery (Figure 4B). The persistence of these changes in the *ex vivo* setting suggests that a
204 single episode of PEM induced fixed regulatory alterations, leading to the observed long-
205 lasting transcriptional changes.

206

207 **Integrative Analysis of Genome-Wide DNA Methylation and Differential Gene Expression in**
208 **Small Intestinal Epithelial Cells During Acute PEM and Post-Recovery**

209 DNA methylation is an epigenetic mechanism that plays a key role in the long-term regulation
210 of gene expression. In our previous work, we demonstrated its involvement in the
211 differentiation processes of intestinal epithelial cells [32,34]. To find a potential mechanism of
212 the observed long-lasting transcriptional memory effect after PEM, we next analyzed
213 genome-wide DNA methylation signatures by bead-based arrays using purified intestinal
214 epithelial cells from the small intestine at acute PEM (4 weeks) and after recovery (10 weeks)
215 and respective controls. In the acute PEM samples, we identified 33,013 differentially
216 methylated positions (DMPs), of which 18,214 were hyper- and 14,799 hypomethylated
217 (Figure 4C). Whereas after recovery, hypomethylation was the prevailing pattern compared
218 to age-matched controls (21,753 hypo- vs. 9550 hypermethylated sites). Similar to the
219 intersection of transcriptome signatures shared by acute PEM and recovery samples, we
220 found that a notable proportion of DMPs from acute PEM overlapped with DMPs detected in
221 the recovery group, with 1026 hyper- and 1007 hypomethylated sites being persistently
222 deregulated (Figure 4D). Differentially methylated sites significantly overlapped with binding
223 motifs for several transcription factors, for example the cell division proteins and PPAR targets
224 RAD21 and SMC3 [35,36], as well as the mRNA transporter ZC3H11A and transcriptional
225 repressor CTCF which were enriched in hypomethylated sites shared between acute PEM and
226 recovery samples (Figure 4E).

227 To delineate regulatory DNA methylation changes linked with persistently altered gene
228 expression *in cis*, we integrated transcriptome and methylome data using a hierarchical
229 approach as described [32,37] (Figure 4F). First, we located DMPs situated within a range of 5kb
230 before or after the transcription start site of any DEG. Next, we computed the correlation
231 between the expression level of each DEG and the intensity of methylation at the
232 corresponding DMPs. Among 56,271 deregulated DMPs analyzed, 6,554 were located within
233 the defined window of at least one DEG. Out of these, 6,197 DMP-DEG pairs representing
234 3,394 genes exhibited significant correlation, with 51% displaying a reciprocal correlation (i.e.,
235 high methylation linked to low transcript levels or vice versa) and 49% exhibiting a
236 cooperative correlation (i.e., high methylation linked to high transcript levels or vice versa).
237 31 DMP-DEG with a persistent pattern in acute PEM and after recovery were identified (Figure
238 4G). We were able to identify persistent links between DNA methylation and transcriptome
239 signatures, both after acute PEM and in the recovery phase. The cis-linked DNA methylation-
240 DEG pairs point towards potential long-term alteration of cellular states through epigenetic
241 regulation after a PEM episode. Notably, GDF15 (Growth/Differentiation Factor 15) emerged
242 as a promising candidate for mediating some of the long-term PEM memory effects, given its
243 established role as an endocrine signal of nutritional stress and body mass regulation and as
244 a mediator of cancer cachexia [38–40.]

245

246 **Intestinal microbial community dynamics in acute PEM and after recovery indicate a high**
247 **level of resilience to PEM-induced perturbation**

248 To explore the potential involvement of gut microbial dysbiosis for the observed sustained
249 phenotypes, we performed 16S rRNA gene sequencing on sequential stool samples collected
250 from mice during the PEM-recovery experiment (Figure 5A). During PEM (up to week 4),
251 bacterial α-diversity as measured by the Shannon Index declined significantly compared to
252 control-fed mice, but fully normalized again after switching to control diet during recovery
253 (from week 5 to 10) (Figure 5B). Composition of the fecal microbiota from mice of under acute
254 PEM differed profoundly from baseline (before dietary intervention) or control-fed
255 littermates (both at 4 weeks and 10 weeks "), and PEM-recovery mice at 10 weeks
256 (PERMANOVA on between-sample Bray-Curtis dissimilarities, F-statistics = 25.5, R^2 = 0.54, p =
257 1e-4, Figure 5C). Specifically, in mice subjected to PEM, *Enterobacteriaceae*, a family of the

258 class Proteobacteria that includes opportunistic pathogenic microorganisms such as
259 *Escherichia* and *Shigella*, which have been linked with infection-related pathologies in
260 malnourished individuals [41,42], were expanded along with *Bacteroides*, *Parabacteroides* or
261 *Lachnospiraceae* UCG-006. In contrast, the relative abundance of *Bifidobacterium*, *Bilophila*,
262 *Lachnospiraceae* NK4A136, *Lachnoclostridium*, *Alistipes*, *Parasutterella*, *Faecalibaculum* and
263 *Muribaculaceae* were significantly decreased (Wilcoxon rank sum test, $p < 0.001$) compared
264 to control-fed mice (Figures 5D and S4A, S4B). No significant differences were observed at the
265 taxonomical level between PEM-recovery mice and their littermate controls. Notably, the
266 intraclass correlation coefficient (ICC), which measures the similarity among samples within
267 the same group, was significantly higher in fecal samples from mice with acute PEM compared
268 to all other experimental groups (Figure S4D). This suggests that acute PEM induces uniform
269 changes in the microbiota, with minimal influence from individual baseline condition or other
270 environmental factors. Through shotgun metagenomic sequencing at weeks 4 and 10, we also
271 explored changes of the functional potential of the microbiome. At 4 weeks, we found that a
272 wide range of metabolic functions related to fatty acid and amino acid metabolism were
273 enriched in the microbiome of mice under acute PEM compared to control-fed mice. (Figure
274 5E and S4C). Again, after recovery at week 10, no significant changes compared to control
275 mice were observed, suggesting that adult microbial communities exhibit strong resilience to
276 this type of perturbation.

277

278 **Lack of an intestinal microbiome ameliorates phenotype severity and alters fecal**
279 **metabolite patterns upon PEM perturbation**

280 We next explored the role of the microbiome in shaping PEM-related phenotypes in our
281 mouse model. We hypothesized that, similar to other stressors like DSS or radiation-induced
282 enteritis [43], the absence of intestinal microbes—which induces an energy-restricted state,
283 particularly in the intestinal mucosa—would exacerbate PEM symptoms. We thus performed
284 the same PEM-recovery diet intervention in germfree (GF) mice of the same genetic
285 background. Contrary to our expectation, GF mice exhibited significantly less body weight loss
286 than conventionally raised (CONV-R) mice with a normal microbiome (Figure 6A). PEM-
287 induced body weight loss could be fully normalized during recovery after switching to a
288 control diet in GF, but not in CONV-R mice (Figure 6A). Importantly, in contrast to CONV-R

289 mice, numbers of Paneth cells were not affected by PEM in the absence of a microbiota
290 (Figure 6B). Organ measures and abundance of other cell types were also unaltered by PEM
291 in GF mice (Figure S5). Untargeted metabolomics of fecal samples from GF and CONV-R mice
292 during acute PEM (day 28, week 4) revealed that lipid metabolites were significantly impacted
293 by the nutritional challenge in a microbiota-dependent manner (Figure 6C). Specifically,
294 conjugated linoleic acids and oxylipins such as 12,13-diHOME and 9-HODE were strongly
295 induced under acute PEM in CONV-R mice, but were virtually absent in GF mice as individually
296 validated by targeted quantitative metabolomics (Figure 6C, D). Supporting this metabolomic
297 data, abundances of the respective functional genes in the microbiome, namely of
298 lipoxygenases (LOX) and epoxide hydroxylases (EH), which generate 9-HODE and 12,13-
299 diHOME from linoleic acid, respectively, were increased under acute PEM only in CONV-R
300 mice as revealed by shotgun metagenomics (Figure 6E). Importantly, using publicly available
301 metagenomic data of malnourished children undergoing a nutritional intervention with either
302 a Microbiota Directed Complementary Food (MDCF-2) or standard Ready-to-Use
303 Supplementary Food (RUSF) [10], we found that abundances of microbial LOX and EH genes
304 declined during the therapeutic nutritional intervention (Figure 6F). These findings
305 collectively demonstrate that fecal oxylipins, such as 9-HODE and 12,13-diHOME, along with
306 the microbial enzymes that produce them, are highly sensitive to protein-energy malnutrition
307 (PEM).
308

309 **Activation of the PPAR-GDF15 pathway disrupts Paneth cell development during PEM**

310 Oxylipins like 12,13-diHOME and 9-HODE are recognized as peroxisome proliferator-activated
311 receptor (PPAR) agonists, and Paneth cell differentiation is regulated by PPAR signaling. We
312 hypothesized that these microbially-derived metabolites may serve as a mechanistic link
313 between the gut microbiota and disruptions in Paneth cell function [44–47]. PPARs are nuclear
314 lipid-activable receptors controlling a variety of genes regulating metabolism, including
315 GDF15 [48,49]. Strikingly, we observed that the expression patterns of both *Gdf15* and *Pparg*
316 were co-dependent on PEM and the microbiome, showing upregulation in response to PEM
317 and during recovery in CONVR mice, but not in GF mice (Figure 7A). We next assessed the
318 functional role of PPAR activation and GDF15 for Paneth cell differentiation. Paneth cell
319 differentiation was induced by a switch to standard [50] ENR-CD medium containing CHIR99021

320 (a GSK3 inhibitor/WNT activator) and DAPT (a γ-secretase inhibitor) (Figure 7B). Successful
321 induction was reflected by increased expression of Paneth cell markers over time, such as
322 Lyz1 (Figures 7C, D, E) and Defa5 (Figure 7C). We first tested the effects of GDF15 on Paneth
323 cells *in vitro*. Strikingly, stimulation of intestinal organoids with recombinant and TGFβ-free
324 GDF15 (rGDF15) [51] resulted in downregulation of Paneth cell markers (Figure 7C). To further
325 explore the link between PPAR signaling and GDF15, we established an *in vitro* organoid PEM
326 model. Intestinal organoids were cultured in either normal or protein-reduced ENR medium
327 (see methods), while simultaneously inducing Paneth cell differentiation by CHIR99021 and
328 DAPT addition. Of note, when organoid cultures were treated with Lanifibranor, a pan-PPAR
329 agonist, under PEM conditions, Paneth cell marker expression was significantly repressed
330 (Figure 7D), while Lanifibranor in the absence of protein restriction had no discernible effect.
331 Additionally, Lanifibranor increased *Gdf15* expression, confirming it as a direct downstream
332 target of PPAR under PEM (Figure 7D). Similar effects were observed with the microbial PPAR
333 agonist 9-HODE *in vitro* under PEM conditions. After 96 hours, 9-HODE decreased *Lyz1*
334 expression and upregulated *Gdf15* after 48 hours (Figure 7E). The timing of events, with an
335 initial upregulation of *Gdf15* expression followed 48 hours later by a decrease in *Lyz1* marker
336 expression in response to 9-HODE stimulation, collectively still supports a mechanistic link.
337 The interaction of PEM and PPAR-GDF15 activation was required to induce defective Paneth
338 cell differentiation as stimulation with Lanifibranor or 9-HODE in the absence of PEM did not
339 reduce *Lyz1* or *Gdf15* expression (Figure S6). These findings therefore suggest the presence
340 of a host-intrinsic PPAR-GDF15 pathway in the intestinal epithelium which can be activated
341 by microbially-derived oxylipin metabolites during PEM and mediates sustained effects on
342 Paneth cell differentiation and function.

343 **Discussion**

344 PEM remains a major global health challenge, impacting millions of individuals worldwide. In
345 recent decades most studies have focused on understanding acute protein undernutrition.
346 Major achievements are based on using locally available ingredients and co-targeting the
347 intestinal microbiome [5,8,10,11,25,52–57]. However, the exact nature of the interactions between
348 the intestinal microbiota and host tissues during nutritional stress are still largely unknown.
349 In this study, we utilized a murine model of adult PEM to systematically investigate the long-
350 term effects of a single severe episode of protein deficiency on both the structure and
351 function of the intestinal mucosa, as well as its associated microbiota. Using multi-omics
352 profiling, we uncovered extensive transcriptional, epigenetic, metabolic, and cellular effects
353 of acute malnutrition. Our findings provide a resource of mucosa-microbiota alterations in
354 the acute phase of PEM, which significantly extends previous insights and can be leveraged
355 to mine for novel targeted interventions [5,8,9,11,58–61]. Importantly, we show that a single
356 episode of PEM leads to a prolonged reduction in body weight and induces significant
357 structural changes in the intestinal epithelium. These include macroscopic alterations, such
358 as a shortened small intestine, and microscopic changes, such as a depletion of Paneth cells,
359 which is a common feature of environmental enteric dysfunction (EED) in malnourished
360 children [62,63]. Paneth cells are key regulators of intestinal physiology and antimicrobial
361 responses, thus, our findings of permanently impaired Paneth cell function due to PEM could
362 potentially explain the increased susceptibility towards gastrointestinal pathogens, i.e.
363 *Enterobacteriaceae*, accounting for severe diarrhea, transmigration peritonitis and sepsis
364 observed in severely malnourished humans [22,23]. The structural changes were accompanied
365 by "memory-like" transcriptional alterations in the intestinal epithelium, notably a prolonged
366 reduction in the expression of key Paneth cell genes, including those encoding antibacterial
367 factors such as defensins and lysozyme, during and after acute PEM. These gene expression
368 changes were sustainably present even in intestinal organoids grown from intestinal stem
369 cells of mice harvested during acute PEM or recovery, when cultured for multiple passages *in*
370 *vitro* under full-nutrient conditions. This suggests the involvement of long-term regulatory
371 mechanisms, such as alterations in DNA methylation [64,65], which control the lasting effects of
372 PEM. Indeed, we could show a strong remodeling of DNA methylation patterns upon PEM in
373 purified intestinal epithelial cells. We conducted an interaction analysis between gene

374 expression and differentially methylated positions [32,37] and identified, besides other
375 differentiation factors (e.g. Neurod1 [66]), a link between cis-linked methylation changes and
376 upregulation of mRNA levels of the pleiotropic stress-induced cytokine GDF15 as a potential
377 mediator of PEM on intestinal function and metabolic processes [67–69].
378 To assess the dynamics of gut microbial community shifts during and after PEM we conducted
379 16S rDNA and metagenomic shotgun sequencing. In line with previous studies [5,7–9,11,58,61] we
380 detected a significant shift of gut microbiota composition and functional potential during
381 acute PEM. Strikingly, PEM-dependent changes completely reverted back to their original
382 configuration during recovery indicating a high level of resilience of fecal microbial
383 communities[70]. We initially hypothesized that lack of microbiome would increase PEM
384 susceptibility, e.g. due to an energetic restriction in the absence of bacterial fermentation [71,72]
385 or lack of TLR-dependent protective signals[43] . Surprisingly, when subjecting GF mice to PEM,
386 we found a significantly milder gastrointestinal phenotype with a less pronounced
387 bodyweight loss, and neither a long-lasting reduction of bodyweight nor significant depletion
388 of Paneth cells. These findings indicate that a second microbially-dependent hit is required to
389 trigger a strong PEM phenotype. Using metabolomics in CONV-R and GF mice, we identified
390 the fecal oxylipin metabolites 12,13-diHOME and 9-HODE as potential sources of the PEM-
391 and microbiome-dependent phenotype. By analyzing metagenomic data, we found increased
392 abundances of LOC and EH genes encoding enzymes that generate 9-HODE and 12,13-
393 diHOME from linoleic acid under acute PEM in CONV-R mice and in malnourished children,
394 which suggests that the same mechanism functions in mice and humans. Both, 9-HODE and
395 12,13-diHOME, have been implicated as immunomodulatory lipids, which may act through
396 PPARs [73–75]. Using an *ex vivo* malnutrition model in intestinal organoids, we then found that
397 protein deprivation alone did not impair Paneth cell differentiation, but a second (microbial)
398 hit targeting the PPAR/GDF15-axis was required.
399 Our data indicate that the sustained loss of Paneth cells could be linked to an epigenetically
400 fixed upregulation of GDF15 in intestinal epithelial cells. Whereas the intestinal epithelium
401 has been shown to be the major site of inducible GDF15 [76] upon nutritional stressors, there
402 are conflicting results on the expression distribution of its cognate receptor glial cell line-
403 derived neurotrophic factor family receptor α-like (GFRAL) as well as on biological effects of
404 yet unidentified non-GFRAL GDF15 receptors. Although the specific receptor system involved
405 was not identified in our study, we used a recombinant GDF15 source, which ruled out the

406 possibility of co-purified TGF being responsible. This suggests that the observed effects are
407 directly attributable to GDF15 itself. Our findings are of particular clinical relevance as biologic
408 treatments targeting GDF15 have not only proven effective in mice [77], but they are currently
409 entering phase 2 clinical trials for tumor cachexia in patients [40,78]. While the main effect of
410 this new drug class is to increase bodyweight via enhanced appetite, muscle function and
411 physical performance, these drugs could also prove effective in restoring Paneth cell numbers
412 and function in malnourished patients, thereby alleviating gastrointestinal symptoms and
413 reducing PEM lethality. A major obstacle in a global use of biologicals for PEM will be the
414 expected high cost of therapy. Instead, targeting the microbial metabolites 12,13-diHOME or
415 9-HODE could provide a cost-effective alternative significantly extending the scope of
416 successful nutritional interventions targeting the intestinal microbiome [10].

417

418 **Potential limitations of the study**

419 This study was conducted using a single episode of PEM in an adult murine model. Even
420 though there is evidence that these findings can be translated to the human situation (e.g.
421 Paneth cell disruption, elevated GDF15 levels, elevated abundance of LOX/EH genes), our
422 comprehensive molecular profiling results pointing towards a long-term memory-like effect
423 of PEM remain to be validated in a human setting. Moreover, studies on the relevance of our
424 findings for the childhood situation, e.g. for developmental phenotypes such as stunting [2], are
425 warranted. In addition, like most controlled PEM studies we used an isocaloric set-up, which
426 does not reflect the usual undernutrition scenario in crisis regions, where both available
427 protein and overall calories are severely reduced. It must be emphasized that the alteration
428 of lipid metabolism, which we see both in the mucosal transcriptome and bacterial
429 metagenome, is not linked to increased lipid content of the synthetic diet, as protein calories
430 are replaced by carbohydrates. Since lipid metabolism has been shown to be altered in human
431 malnutrition cohorts through both microbiome and serum analyses [79–82], we are confident
432 that the observed changes are primarily driven by metabolic shifts resulting from limited
433 protein availability. Importantly, due to our experimental setup, we do neither address the
434 effects of multiple PEM periods nor the duration of the observed memory phenotype in the
435 intestinal epithelium. From earlier regeneration kinetics, it seems however unlikely that the
436 effect is simply caused by the physiological lag time of differentiation, as acute chemical

437 ablation of Paneth cells was followed by re-appearance of mature cells already after 24h [83] .
438 An interesting explanation for the disappearance of Paneth cells could be a permanent trans-
439 differentiation to stem-like dividing cells, which could partially replace the original stem cells
440 [84,85]. Further follow up studies including longer observation periods and/or multiple PEM
441 episodes and single cell-based analyses are required to comprehensively study the effects on
442 epithelial lineage decisions, but also long-term effects in other cell types and tissue
443 compartments.
444 It is increasingly evident that phenotypic responses to PEM vary between the sexes [86]. In our
445 study, most analyses have been done in males. In the GF condition, we included both sexes
446 and observed no significant differences between them. Further research should therefore
447 investigate sex-dependent effects during PEM, especially since woman during pregnancy and
448 breast-feeding are a very vulnerable group of patients prone to suffering from PEM due to an
449 increased protein demand [87]. Moreover, in this study we utilized a PEM model characterized
450 by a general protein deficiency, rather than a shortage of specific amino acids or their
451 combinations. Certain amino acids, such as tryptophan, undergo extensive metabolism by
452 both the host and the microbiota, generating metabolites with diverse signaling roles in
453 immune regulation and differentiation processes. These metabolites are known to influence
454 the expression of antimicrobial peptides [25,88]. It will be crucial to investigate whether the
455 acute and memory-like effects of PEM can be reversed through supplementation of these
456 amino acids or their metabolites, such as those involved in the kynurenine/nicotinamide
457 pathway.
458
459 **Conclusions**
460 In this study we present a comprehensive multi-omics resource of a dietary PEM model in
461 mice, revealing that a single episode of PEM induces long-lasting phenotypic changes, with a
462 particular focus on the intestinal mucosa and microbiota. Key findings include sustained
463 weight loss, shortening of the small intestine, impaired proliferation of intestinal epithelial
464 cells, a reduction in Paneth cells, and diminished expression of genes encoding antimicrobial
465 agents. Notably, germ-free (GF) mice exhibited alleviated acute PEM symptoms and did not
466 manifest any of the aforementioned long-term PEM-associated phenotypic changes. Through
467 an integrative multi-omics analysis and *ex vivo* intestinal organoid stimulations, we identified
468 microbial lipid metabolites, such as 12,13-diHOME and 9-HODE, along with the host PPAR-

469 GDF15 axis, as potential molecular drivers of the enduring PEM phenotype, particularly the
470 dysfunction of Paneth cells. These findings suggest that targeting microbial lipid production
471 or the host GDF15 pathway could provide novel therapeutic strategies, not only for
472 malnutrition, but also for other conditions associated with Paneth cell dysfunction, such as
473 Crohn's disease [89,90].

474 **Methods**

475 **Animals.** All animal experiments were approved by the local animal safety review board of
476 the federal ministry of Schleswig Holstein and conducted according to national and
477 international laws and policies (V242-30405/2016(55-5/16), V242-6900/2019(28-3/19) and
478 V242-60285/2019(105-9/19)). C57Bl6/J mice were purchased from Charles River Laboratories
479 and housed in the Central Animal Facility (ZTH) of the University Hospital Schleswig Holstein
480 (UKSH, Kiel, Germany) under specific-pathogen free (SPF) conditions in individually ventilated
481 cages (Green Line, Techniplast) or under sterile conditions in gnotobiotic flexible film isolators
482 at the Max Planck Institute for Evolutionary Biology in Plön. All mice were kept under a 12-h
483 light cycle and fed a regular gamma-irradiated chow diet *ad libitum*.

484 **Dietary PEM intervention experiment.** All custom PEM and CTRL diets were purchased from
485 Ssniff (Table S1). To induce PEM in adult mice, 10-week-old CONV-R or 10-16-week-old GF
486 C57Bl6/J mice (n=40) were either given a control diet (CTRL, 20% protein) or an isocaloric diet
487 with reduced protein content (PEM, 0.7% protein) for 4 weeks to induce an acute PEM. To
488 induce PEM in young mice, 4-week-old C57Bl6/J mice (n=40) were either given a control diet
489 (CTRL, 20% protein) or an isocaloric diet with reduced protein content (PEM, 2% protein due
490 to a greater PEM susceptibility of young mice) for 4 weeks to induce an acute PEM. One half
491 of each experimental group was killed for blood & organ harvest at 4 weeks to assess the
492 acute PEM phenotype. The other half of the experimental groups was either kept on or
493 switched to a diet with regular protein content for an additional six weeks to assess recovery
494 from PEM. Up to five recipient mice were co-housed. Mice were weighed every week and
495 fecal pellets were collected, immediately frozen on dry ice and stored at –80°C. For final
496 analyses, blood was collected from the vena cava, mice were killed by cervical dislocation and
497 tissues were removed for histological and molecular analyses.

498 **Histology and immunostainings.** Tissue specimen were fixed in methacarn (60% dry
499 methanol, 30% dry chloroform, 10% glacial acetic acid) for 1-2 weeks at room temperature
500 prior to paraffin embedding and sectioning. 5 µm thick sections were cut and deparaffinized
501 in Roti-Histol and rehydrated in ethanol followed by hematoxylin and eosin (H&E) or periodic
502 acid-Schiff (PAS, TH Geyer, 3952016) staining. Alternatively, sections were boiled in citrate
503 buffer for antigen retrieval and subjected to immunostaining. For this purpose, we used the
504 Vectastain ABC kit (Vector Laboratories), peroxidase-substrate solution from DAB Peroxidase

505 (HRP) Substrate Kit (Vector Laboratories) and primary antibodies for detecting proliferating
506 cells were incubated in a 1:500 diluted mouse anti-Ki67 antibody (BD Biosciences, cat.no.
507 556003) and for Paneth cells in a 1:500 diluted mouse anti-LYZ1 antibody (Santa Cruz, cat.no.
508 sc-27956) overnight at 4°C. TUNEL assay was performed with the *in situ* cell death detection
509 Kit, TMR red (Roche, 12156792910) according to the manufacturer's instructions, while nuclei
510 were counterstained with DAPI (4',6-diamidino-2-phenylindole, dihydrochloride) nuclear dye
511 (Thermo Fisher, 62247). Slides were visualized using a Zeiss Imager Z1 microscope (Zeiss) and
512 pictures were taken using ZEN pro (Zeiss) software.

513 **Isolation of intestinal epithelial cells (IECs).** IECs were isolated from small intestinal tissue
514 using the Lamina Propria Dissociation Kit (Miltenyi BioTech, Bergisch Gladbach, Germany)
515 according to the manufacturer's protocol. In brief, intestinal epithelial cells were isolated by
516 disruption of the structural integrity of the epithelium using ethylenediaminetetraacetic acid
517 (EDTA) and dithiothreitol (DTT). Purity of individual IEC fractions was analyzed by flow
518 cytometry on a FACS Calibur flow cytometer (B&D, Heidelberg, Germany) with Cellquest
519 analysis software from Becton Dickinson. We used the Anti-EpCam-PE (Clone: G8.8,
520 Biolegend, San Diego, USA) antibody for analysis of IEC purity.

521 **Noggin-conditioned medium.** HEK Noggin cells, previously described by Miyoshi and
522 Stappenbeck (2013) and provided by Prof. Zeissig's group at CRTD, Dresden University,
523 Germany, were used in this study. In summary, HEK cells were modified to secrete Noggin
524 protein into the culture medium. The cells were thawed in DMEM + 10%(v/v) FBS purchased
525 from Biochrom. Once confluent, the cells were cultured for 3 cycles in DMEM with 10% (v/v)
526 FBS and 10 µg/mL Puromycin (Sigma-Aldrich). After the 3rd cycle, the cells were diluted 1:20
527 and cultured in DMEM with 10% (v/v) FBS without Puromycin. Four days later, the medium
528 was collected and centrifuged to remove excess cells. Fresh DMEM with 10% (v/v) FBS was
529 added and after another four days, the second batch of medium was collected and
530 centrifuged. The medium from the first batch was then combined with the second batch.

531 **R-Spondin-conditioned medium.** HEK R-Spondin-1-producing cells, previously described by
532 Miyoshi and Stappenbeck (2013) and provided by Prof. Zeissig´s group at CRTD, Dresden
533 University, Germany, were used in this study. In summary, HEK cells were modified to secrete
534 R-Spondin-1 protein into the culture medium. The cells were thawed in DMEM with 10% (v/v)
535 FBS (Biochrom). Once confluent, the cells were cultured for 3 cycles using DMEM with 10%

536 (v/v) FBS+ 300 µg/mL Zeocin (Thermo Fisher). After the 3rd cycle cells were diluted 1:20 and
537 cultured in DMEM with 10% (v/v) FBS without Zeocin. Four days later, the medium was
538 collected and centrifuged to remove excess cells. Fresh DMEM with 10% (v/v) FBS was added
539 and after another four days, the second batch of medium was collected and centrifuged. The
540 medium from the first batch was then combined with the second batch.

541 **Isolation and culture of intestinal organoids.** Organoids were generated from small intestinal
542 crypts of male C57Bl6/J mice receiving either a control or PEM diet following procedures
543 described earlier by Sato et al., 2009 [91]. Organoids were cultivated in 24 well plates at 37°C
544 with 5% CO_2 atmosphere in Matrigel (BD) with ENR-conditioned medium supplemented with
545 0.1% human recombinant EGF (50 µg/mL) as described by Sato et al., 2011 [50]. ENR-
546 conditioned medium consisted of 70% (*v*/*v*) 2 × basal medium (Advanced DMEM/F12
547 supplemented with HEPES [1M], Glutamax [100×], Penicillin/streptomycin 10,000 U/mL
548 [1:50] and N-Acetylcysteine [500 mM]), 10% (*v*/*v*) Noggin-conditioned medium and 20% R-
549 Spondin-conditioned medium.

550 **Organoid PEM model.** Murine **i**ntestinal organoids were initially cultured for 48 h in ENR-CV
551 medium, an ENR-conditioned medium containing 3.3 µM CHIR99021 (Miltenyi Biotech, #130-
552 103-926) and 1 mM valproic acid (Sigma, PHR1061-1G) promoting differentiation into the
553 stem cell niche. These stem cell organoids were then transitioned to either ENR-CD or PEM-
554 CD medium containing 3.3 µM CHIR99021 and 10 µM DAPT (Tebubio, 25704-0041) to further
555 drive differentiation into the Paneth cell niche.

556 The PEM culture medium (1.25% amino acids) consisted of 68.75% (*v*/*v*) Advanced DMEM/F12
557 (ADF) medium without amino acids or glucose [Biozol/US Biological Life Sciences, #USB-
558 D9800-27-10] supplemented with 10 mM HEPES, 1× Glutamax, 100 U/mL
559 Penicillin/streptomycin and 1 mM N-Acetylcysteine), 1.25% (*v*/*v*) regular ADF medium with
560 full amino acid concentrations, 10% (*v*/*v*) dialysed Noggin-conditioned medium and 20%
561 dialysed R-Spondin-conditioned medium. The Noggin- and 20% R-Spondin-conditioned media
562 were dialyzed using using cellulose-hydrate tubing with a cutoff of 15 kDa (Reichelt
563 Chemietechnik GmbH, catalogue number 84605)) to prevent the introduction of nutrients
564 from the added conditioned media while retaining Noggin and R-Spondin required for
565 organoid growth. for the in-vitro PEM model the conditioned Medium was dialized. Dialysis
566 success was assessed using Multistix 10 SG testing strips (Siemens).

567 **Organoid stimulations with GDF15, Lanifibranor or 9-HODE.** Murine intestinal organoids
568 were initially cultured for 48 h in ENR-CV medium, an ENR-conditioned medium containing
569 3.3 µM CHIR99021 (Miltenyi Biotech, #130-103-926) and 1 mM valproic acid (Sigma,
570 PHR1061-1G) promoting differentiation into the stem cell niche. These stem cell organoids
571 were then transitioned to either ENR-CD or PEM-CD medium containing 3.3 µM CHIR99021
572 and 10 µM DAPT (Tebubio, 25704-0041) to further drive differentiation into the Paneth cell
573 niche. Organoids were divided into experimental groups and stimulated with 1 µg *E. coli*
574 derived recombinant mouse GDF15 (R&D Systems, 8944-GD) per 500 µl organoid medium for
575 up to 120h, 20 µM of the pan-PPAR agonist Lanifibranor (MedChemExpress, HY-104049) for
576 24h to 96h or 1 µM 9(S)-HODE (Sigma Aldrich, SML0503) for 24h to 96h. Corresponding
577 control groups received vehicle treatments identical to those used for the stimuli. All
578 organoids were then cultured as described above.

579 **RNA isolation and qPCR.** RNA was extracted using the RNeasy Mini Kit (QIAGEN) according to
580 the manufacturer's protocol. Total RNA concentration was determined with a NanoDrop ND-
581 1000 spectrophotometer (PeqLab Biotechnologie). Total RNA was reverse transcribed to
582 cDNA using the High-Capacity cDNA Reverse Transcription Kit (ThermoFisher Scientific,
583 4368814). qPCR was carried out using TaqMan® Gene Expression Assays (ThermoFisher
584 Scientific) (Table S2) according to the manufacturer's instructions on a Viia 7 Real-Time PCR
585 System (ThermoFisher Scientific). Relative gene expression was normalized to housekeeper
586 gene *Actb* (β-actin) and calculated by the $2^{-\Delta Ct}$ method.

587 **Transcriptional profiling by RNA sequencing.** Total RNA from IECs and intestinal organoids
588 was extracted using the RNeasy Mini Kit (Qiagen) according to the manufacturer's protocol.
589 RNA concentration and integrity were analysed using a TapeStation 4200 System (Agilent)
590 and a Qubit 4 fluorometer (ThermoFisher Scientific). RNA-sequencing libraries were prepared
591 using the TruSeq® RNA seq Library Prep Kit v2 according to the Illumina TruSeq® messenger
592 (mRNA) sequencing protocol. The RNA-seq libraries were sequenced on an Illumina HiSeq
593 4000 sequencer (Illumina, San Diego,CA) with an average of 23 million reads (1x 50 bp) at
594 IKMB NGS core facilities. The nf-core rnaseq pipeline (version 1.2) (https://github.com/nf-
595 core/rnaseq) [92] was used to pre-process the sequencing data. Adapter and low-quality bases
596 from the sequencing reads were trimmed using Trim Galore (0.5.0)
597 (http://www.bioinformatics.babraham.ac.uk/projects/trim_galore/) and reads shorter than

598 35bp after trimming were removed. The filtered genes were mapped to the mouse genome
599 (GRCm38) using STAR aligner (version 2.6.1a) [93]. The expression counts of the genes were
600 estimated using featureCounts (version 1.6.2) [94] and were normalized across samples using
601 the DESeq normalization method. Differentially expressed genes (DEGs) between Ctrl_4w and
602 PEM_4w samples as well as Ctrl_10w and Recovery 10w samples were identified using the
603 Bioconductor package DESeq2 (version 1.20.0) [95]. Genes with FDR adjusted p-value of 0.05
604 were regarded as differentially expressed (DEGs). Gene ontology enrichment analyses were
605 conducted using the Bioconductor package topGO (version 2.46.0) [96] with genes with similar
606 expression level as the universe set. In the topGO analysis, the Fisher.elim p-value, calculated
607 using the weight algorithm, of 0.05 was used as the significance threshold.

608 Transcription factor binding sites (TFBS) enriched in the promoter regions of DEGs were
609 identified by conducting enrichment analysis using the Bioconductor package LOLA (version
610 1.24.0) [97]. Promoter regions were defined as the region between 1,500 bp upstream to 500
611 bp downstream of the transcription start site.

612 **Spatial transcriptomics.** Small intestinal tissue was prepared for spatial transcriptomics using
613 the Visium Spatial Fresh Frozen Protocol CG000240 (RevE, 10x Genomics). Briefly, small
614 intestinal tissue was rolled into Swiss rolls, embedded in O.C.T. medium (Tissue-Tek) within
615 Cryomolds (Tissue-Tek), and then rapidly immersed in pre-cooled isopentane on liquid
616 nitrogen until the O.C.T. medium solidified. The samples were subsequently cryopreserved at
617 -80°C. To determine the optimal permeabilization time of 15 minutes, serial 10µm sections
618 were cut and mounted on a Visium Tissue Optimization Slide (10x Genomics). For spatial
619 transcriptomics, additional 10µm-thick sections were mounted on a Visium Gene Expression
620 Slide for Fresh Frozen (10x Genomics), followed by methanol fixation and H&E staining
621 following protocol CG000160 (RevD, 10x Genomics). Whole slide imaging was conducted
622 using a NanoZoomer S60 Digital Slide Scanner (Hamamatsu, C13210-04) with 40x
623 magnification. Spatial library construction was carried out according to the manufacturer's
624 protocol CG000239 (RevH, 10x Genomics), and the libraries were then sequenced on a
625 NovaSeq 6000 sequencer (Illumina) with 2x 100bp read length. Sequencing data was mapped
626 to the mouse reference genome (mm10) using 10x spaceranger v.2.1. Feature-barcode
627 matrices for each sample were imported into the R package 'Seurat' v.4.2.0 for quality control,
628 normalization, dimensionality reduction, and Louvain clustering [98]. As quality control, spots

629 were filtered if they had <200 features (genes) or >25% of mitochondrial gene expression.
630 After spot filtration, sample level normalization was performed using SCTransform [99] function
631 in Seurat, which uses a regularized negative binomial regression to transform the UMI count
632 data. Thereafter, sample integration was performed with the CCA algorithm followed by a
633 Shared Nearest Neighbor (SNN) construct graph and clustering using default settings. Using
634 high-resolution images of H&E-stained intestinal Swiss roles, multiple regions were identified,
635 and spots classified as belonging to “Crypt”, “Muscle”, “Villus-Intermediate” (including both
636 bottom and middle sections), or “Villus-Tip” regions. The dominant clusters corresponding to
637 each category were then used for differential gene analysis. The "FindMarkers" function in
638 Seurat v4.2.0 was used to identify differentially expressed genes (DEGs) within each cluster
639 corresponding to Crypts, Villus-Tips, and Villus-Intermediate under both CT and PEM
640 conditions. Genes were classified as upregulated if they had log2 fold changes >0 and as
641 downregulated if they had log2 fold changes <0 with an adjusted p-value <0.05. Gene
642 ontology enrichment analysis of these DEGs was performed using clusterProfiler v4.12.1 [100]
643 with thresholds of adjusted p-value <0.05 (hypergeometric test).

644 **DNA methylation profiling.** DNA was isolated from IECs using the DNeasy Blood and Tissue
645 Kit (Qiagen) according to the manufacturer’s protocol. DNA methylation levels were
646 measured using the Infinium Mouse Methylation BeadChip (Illumina), which covers > 285k
647 methylation sites spanning over CpG islands, transcription start sites, enhancers, and gene
648 regions. DNA methylation data was analysed using the Bioconductor package RnBeads
649 (version 2.12.1) [101]. Sites that overlapped with SNPs and had unreliable measurements were
650 filtered out. Context-specific probes, probes on the sex chromosomes, and probes with
651 missing values were also removed resulting in the removal of 54,378 out of 261,600 probes.
652 The signal intensity values were normalized using the dasen method. Differentially
653 methylated positions (DMPs) and regions (DMRs) between Ctrl_4w and PEM_4w samples as
654 well as Ctrl_10w and Recovery 10w samples were identified using the automatically selected
655 rank cutoff of RnBeads. Predicted transcription factor binding sites (TFBS) enriched in DMPs
656 were identified by conducting enrichment analysis using the Bioconductor package LOLA
657 (version 1.24.0) [97].

658 **Integration of DNA methylation and transcriptome data.** To integrate gene expression data
659 with DNA methylation data, we used a hierarchical approach as described before [32,102]. We

660 first identified DMPs located 5,000 bp upstream and downstream of the transcription start
661 sites of DEGs. Spearman's rank correlation coefficient between the normalized expression
662 count of each DEG and the methylation intensity (β-values) of its corresponding DMPs were
663 calculated. To test the statistical significance of the correlations, we calculated the false
664 discovery rate (FDR) using a permutation approach.

665 **16S rRNA gene amplicon sequencing.** DNA was isolated from fecal material using the DNeasy
666 PowerSoil Kit (Qiagen) following the manufacturer's protocol. Extracted DNA was eluted from
667 the spin filter silica membrane with 100 µl of elution buffer and stored at -80 °C. 16S profiling
668 and MiSeq sequencing was performed as described earlier [103,104], with the following
669 modifications: the V3-V4 region of the 16S rRNA gene was amplified using the dual barcoded
670 primers 319F (ACT CCT ACG GGA GGC AGC AG) and 806R (GGA CTA CHV GGG TWT CTA AT)
671 [105]. Each primer contained additional sequences for a 12 base Golay barcode, Illumina adaptor
672 and a linker sequence [106]. PCR was performed using the Phusion Hot Start Flex 2X Master Mix
673 (NEB) in a GeneAmp PCR system 9700 (Applied Biosystems) and the following program (98°C
674 for 3 min, 25-30x (98°C for 20 s, 55°C for 30 s, 72°C for 45 s), 72°C for 10 min, hold at 4°C).
675 Performance of the PCR reactions was checked using agarose gel electrophoresis.
676 Normalization was performed using the SequalPrep Normalization Plate Kit (Thermo Fisher
677 Scientific, Darmstadt, Germany) following the manufacturer's instructions. Equal volumes of
678 SequalPrep-normalized amplicons were pooled and sequenced on an Illumina MiSeq (2 x 300
679 nt). Quality control of the MiSeq 16S amplicon sequence data was performed in MacQIIME
680 v1.9.1 (http://www.wernerlab.org/software/macqiime) [107]. Sequencing reads were trimmed
681 keeping only nucleotides with a Phred quality score of at least 20, then paired-end assembled
682 and mapped onto the samples using the barcode information. Microbiome phylogenetic
683 analyses were conducted using QIIME2 [108] (release 2022.8). The paired-end sequences were
684 filtered, denoised, and chimera removed using DADA2 [109] plugin resulting in abundance tables
685 of amplicon sequence variants (ASVs) with on average 7.7K ± 4.2K (mean ± sd) reads per
686 sample. Taxonomy was assigned using the Bayesian classifier provided in DADA2 and using
687 the Silva rRNA database v.138 [110]. ASVs not assigned to "Bacteria" or annotated as
688 "Mitochondria", "Chloroplast", or "Eukaryote" were removed. QIIME2 outputs (feature table,
689 taxonomy assignation, and rooted tree), were combined into a single object using the qiime2R
690 (0.99.6) and Bioconductor phyloseq R (1.40.0) [111] packages.

691 **Metagenomic sequencing.** A total of 32 fecal DNA samples (8 Ctrl_4w, 8 Ctrl_10w, 8 PEM_4w,
692 and 8 Recovery_10w), which were already included in the 16S profiling, were also subjected
693 to shotgun metagenomic sequencing performed at the Competence Centre for Genomic
694 Analysis (Kiel). DNA libraries were generated using the Illumina DNA Prep kit following the
695 manufacturer's instructions. Libraries were then pooled and sequenced on an Illumina
696 NovaSeq 6000 with 2 x 150 nt for 19.6 ± 4.14 (mean ± sd) million reads per sample. Shot-gun
697 reads were processed using an in-house established workflow from our institute
698 (https://github.com/ikmb/TOFU-MAaPO) that relies on BBtools and bowtie2 for mapping and
699 host decontamination, and bioBakery tools (MetaPhlAn 4.0 and HUMaN 3.6) for taxonomic
700 and functional potential profiling. Raw reads were quality trimmed and mapped to the mouse
701 genome (GRCm39) to discern between sequenced reads from the host and the gut
702 microbiome bacteria. Only samples containing >1 Gbp after trimming and host
703 decontamination were kept in the analysis. Taxonomic features and microbial relative
704 abundances were determined using MetaPhlAn 4.0 [112] with default parameters and its SGB
705 database containing unique marker genes of 26,970 species-level genome bins (SGBs) derived
706 from a collection curated 1.01M prokaryotic and metagenome-assembled genomes (MAGs).
707 Functional profiles (stratified pathways, gene families and enzyme categories) were
708 computed using HUMAnN 3.6 [113] with default parameters. All abundances were transformed
709 to CPM (count per million) before any statistical analysis.

710 **Microbiome phylogenetic analyses of 16S and metagenomics data.** Uni- and multivariate
711 analyses were performed in R (v.4.2.1) under phyloseq [111] (v.1.40.0), vegan [114] (v.2.6-2) and
712 MAasLin2 [115] (v.1.10.0). All samples for diversity analyses were normalized by rarefaction to
713 the minimum shared read count to account for differential sequencing depth among samples.
714 Relative abundance was calculated by dividing the number of reads for an ASV by the total
715 number of sequences in the sample. Within sample diversity (alpha diversity) was explored
716 using various diversity indexes (Chao1, Shannon, Simpson, Observed ASVs) on ASV abundance
717 data coupled to significance testing (Wilcoxon signed rank test or Kruskal-Wallis tests).
718 Between-sample diversity (beta diversity) as well as differences in diet groups and time were
719 explored and visualized using a Principal Coordinate Analysis (PCoA) plot based on Bray-Curtis
720 distances. Associations of microbiome composition to specified covariates were tested with
721 the implementation of PERMANOVA models (using the adonis2 function from the vegan

722 package). The P and R^2 values were determined by 10,000 permutations using time. To
723 explore variation between and within individuals per diet phase at the genus level, the
724 intraclass correlation coefficient (ICC) was computed by the *ICCest* function of the ICC R
725 package, using as input the longitudinal rarefied abundances, defining each individual mouse
726 as a distinct class. ICC estimation uses the variance components from a one-way ANOVA
727 (between-group variance and within-group variance). To detect differences in the abundance
728 of microbial features (16S rRNA, metagenomics) or pathways (metagenomics) between the
729 experimental groups over time, we built linear mixed models using the MaAslin2 [116] package
730 that included time, diet group and individual mice as a random variable (*microbial*
731 *abundances ~ (1|mouse) + diet switch + time*). P values were corrected for multiple hypothesis
732 testing using the Benjamin-Hochberg procedure, and a false discovery rate <0.05 was defined
733 as the significant threshold. Features (taxa, or pathways) appearing in at least 20% of the
734 samples were included in the analysis.

735 **Identification of genes involved in the bacterial transformation of Linoleic acid-derived**
736 **oxylipins.** Databases of known bacterial oxylipin transformation enzyme genes such as
737 Epoxide hydrolases (~66.000) and Lipooxigenases (~7800) were generated using the NCBI
738 protein database. All genes tagged with the following search criteria were included in the
739 database. (i) Epoxide hydrolases (10th of March, 2023): (epoxide hydrolase[Protein Name] OR
740 (epoxide[All Fields] AND hydrolase[All Fields])) AND (bacteria[filter] AND refseq[filter]). (ii)
741 Lipooxygenases (24th of March, 2023): Lipoxygenase[All Fields] AND bacteria[filter]. The
742 specific enzyme database (Epoxide hydrolases and Lipooxigenases) and the UniRef90
743 database [117] were input into the ShortBRED identify pipeline (v.0.9.5) and used to generate
744 protein-specific markers [118]. These markers along with the quality-controlled metagenomics
745 samples were used as input for ShortBRED quantify to get the presence of copy numbers of
746 the target protein markers.

747 **Non-targeted metabolomics using HILIC UHPLC-MS/MS.** Fecal pellets (~25mg) were weighed
748 in sterile ceramic bead tubes (NucleoSpin® Bead Tubes, Macherey-Nagel, Dueren, Germany)
749 and 1mL of methanol was added (−20°C; LiChrosolv, Supelco, Merck, Darmstadt, Germany).
750 Metabolite extraction was performed with Precellys® Evolution Homogenizer with following
751 settings (4,500 rpm, 40 seconds of 3 cycles with 2 seconds pause time, Bertin Corp., Rockville,
752 Maryland, USA). Samples were centrifuged for 10 minutes at 21,000 × g, cooled at 4°C and

753 900 µL of supernatant was transferred into new tubes. Fifty microliters of supernatant were
754 evaporated (40°C, SpeedVac Concentrator, Savant SPD121P, ThermoFisher Scientific,
755 Waltham, MA, United States) and reconstituted in 75% acetonitrile (ACN; LiChrosolv,
756 hypergrade for LC-MS; Merck KGaA). Samples were analyzed using an UHPLC system (ExionLC,
757 Sciex LLC, Framingham, MA, USA) coupled to a quadrupole time-of-flight mass spectrometer
758 (X500R QTOF MS, Sciex LLC, Framingham, MA, USA). Parameters of the MS for positive and
759 negative electrospray ionization mode are summarized in Table S3 and hydrophilic interaction
760 liquid chromatography (HILIC) was performed as described previously [119] to analyze small
761 polar metabolites.

762 **Targeted metabolomics identification of 9-HODE and 12,13-diHOME.** Identification and
763 semi-targeted peak picking of 12,13-diHOME ((9Z,12S,13S)-12,13-dihydroxyoctadec-9-enoic
764 acid) and 9-HODE was conducted with the same LC-MS method as described previously [120].
765 Here, we used an UHPLC system (ExionLC, Sciex LLC, Framingham, MA, USA) coupled to a
766 quadrupole time-of-flight mass spectrometer (X500R QTOF MS, Sciex LLC, Framingham, MA,
767 USA). We analyzed 12,13-diHOME standard, present on the GUTMLS01-1EA plate (Sigma-
768 Aldrich, Plate 1, Row A, final concentration of around 0.0025 µg/µL, dissolved and diluted in
769 methanol) and fecal extracts of CONVR and GF mice. The identity of 9-HODE was verified by
770 matching against spectral library of MassBank of North America. The X500R QTOF MS was set
771 to negative electrospray ionization mode with parameters summarized in Table S3.

772 **Metabolomics data processing and analysis.** Raw LC-MS (.wiff2) data were post-processed
773 using GeneData Expressionist Refiner MS 15.0 (GeneData GmbH, Basel, Switzerland) including
774 chemical noise subtraction (signal with intensities <200 were removed), chromatographic
775 peak picking, chromatogram isotope clustering, valid feature filter (features present in 10%
776 of samples and at least 500 maximum intensity), retention time range restriction (0.4-9
777 minutes), annotate known peaks (mass-to-charge tolerance of 0.005 Dalton and retention
778 time tolerance of 0.1 minutes), MS/MS consolidation (keep signals with highest total ion
779 count for one cluster in one sample), MS/MS peak detection and export to MASCOT generic
780 files. Processing resulted in a data matrix containing clusters (*m*/*z* and retention time values)
781 and observed maximum intensity values for each sample. Maximum intensity values were
782 normalized to the wet fecal weight. For each cluster we kept MS/MS with highest total ion
783 counts within one sample. MS/MS of clusters across samples were combined with the

784 consensusSpectrum() function of MSnbase (), using mzd of 0.005, minProp of 0.1 and sum for
785 intensityFun argument. Ions of MS/MS were matched with 0.005 Dalton, and intensities of
786 aggregated peaks were summed, if ions were present in minimum 10% of matched spectra.
787 Ions with intensities ≤500 and m/z values ≥ precursor m/z+2 were discarded from consensus
788 spectra. Identification was done by matching experimental MS/MS spectra against spectral
789 libraries, downloaded from MassBank of North America by using MS PepSearch (0.01 Dalton
790 mass tolerance for precursor and fragment Search). Furthermore, GNPS molecular
791 networking and GNPS Library Search was engaged for metabolite identification of
792 experimental MS/MS. Within MS PepSearch output, matches with dot product over 500 were
793 kept and multiple matches for one cluster were filtered for the best match**.** We kept clusters
794 that are present in at least 4 samples and clusters that have valid MS/MS information or
795 metabolite identities. With this approach, we kept 793 and 833 clusters for positive and
796 negative mode, respectively. Furthermore, SIRIUS was used for metabolite identification and
797 classification by an in-silico approach using MS/MS [121]. Multivariate statistical analysis was
798 then performed using Wilcoxon signed rank test implemented in R.

799 **Statistical analysis.** Biostatistical analyses were performed using GraphPad Prism (version 8)
800 software (GraphPad, Inc, La Jolla, CA) or R (v 3.2.5). Specific comparisons and analyses are
801 described in the individual method sections. All pairwise comparisons were performed using
802 Mann-Whitney U test and time-series multiple comparisons were done using Holm-Šídák's
803 multiple comparisons test. Data are shown as mean ± standard error of the mean (SEM).

References

1. World Health Organization (2024). World health statistics 2024: monitoring health for the SDGs, Sustainable Development Goals.
2. UNICEF, WHO, and WORLD BANK (2023). Level and trend in child malnutrition. World Health Organization, 4.
3. Soeters, P., Bozzetti, F., Cynober, L., Forbes, A., Shenkin, A., and Sobotka, L. (2017). Defining malnutrition: A plea to rethink. Clinical Nutrition *36*, 896–901. https://doi.org/10.1016/J.CLNU.2016.09.032.
4. World Health Organization (2000). Turning the tide of malnutrition : responding to the challenge of the 21st century. Preprint at World Health Organization.
5. Smith, M.I., Yatsunenko, T., Manary, M.J., Trehan, I., Mkakosya, R., Cheng, J., Kau, A.L., Rich, S.S., Concannon, P., Mychaleckyj, J.C., et al. (2013). Gut microbiomes of Malawian twin pairs discordant for kwashiorkor. Science (1979) *339*, 548–554. https://doi.org/10.1126/science.1229000.
6. Gordon, J.I., Dewey, K.G., Mills, D.A., and Medzhitov, R.M. (2012). The Human Gut Microbiota and Undernutrition. Sci Transl Med *4*. https://doi.org/10.1126/SCITRANSLMED.3004347.
7. Barratt, M.J., Ahmed, T., and Gordon, J.I. (2022). Gut microbiome development and childhood undernutrition. Cell Host Microbe *30*, 617–626. https://doi.org/10.1016/J.CHOM.2022.04.002.
8. Subramanian, S., Huq, S., Yatsunenko, T., Haque, R., Mahfuz, M., Alam, M.A., Benezra, A., DeStefano, J., Meier, M.F., Muegge, B.D., et al. (2014). Persistent gut microbiota immaturity in malnourished Bangladeshi children. Nature *510*, 417–421. https://doi.org/10.1038/nature13421.
9. Gehrig, J.L., Venkatesh, S., Chang, H.W., Hibberd, M.C., Kung, V.L., Cheng, J., Chen, R.Y., Subramanian, S., Cowardin, C.A., Meier, M.F., et al. (2019). Effects of microbiota-directed foods in gnotobiotic animals and undernourished children. Science (1979) *365*. https://doi.org/10.1126/SCIENCE.AAU4732/SUPPL_FILE/AAU4732_GEHRIG_TABLES-S1-S23.XLSX.
10. Chen, R.Y., Mostafa, I., Hibberd, M.C., Das, S., Mahfuz, M., Naila, N.N., Islam, M.M., Huq, S., Alam, M.A., Zaman, M.U., et al. (2021). A Microbiota-Directed Food Intervention for Undernourished Children. New England Journal of Medicine *384*, 1517–1528. https://doi.org/10.1056/NEJMOA2023294/SUPPL_FILE/NEJMOA2023294_DATA-SHARING.PDF.
11. Barratt, M.J., Nuzhat, S., Ahsan, K., Frese, S.A., Arzamasov, A.A., Sarker, S.A., Munirul Islam, M., Palit, P., Islam, M.R., Hibberd, M.C., et al. (2022). Bifidobacterium infantis treatment promotes weight gain in Bangladeshi infants with severe acute malnutrition. Sci Transl Med *14*, 1107. https://doi.org/10.1126/SCITRANSLMED.ABK1107/SUPPL_FILE/SCITRANSLMED.ABK1107_MDAR_REPRODUCIBILITY_CHECKLIST.PDF.
12. Mostafa, I., Fahim, S.M., Das, S., Gazi, M.A., Hasan, M.M., Saqeeb, K.N., Mahfuz, M., Lynn, H.B., Barratt, M.J., Gordon, J.I., et al. (2022). Developing shelf-stable Microbiota Directed Complementary Food (MDCF) prototypes for malnourished children: study

protocol for a randomized, single-blinded, clinical study. BMC Pediatr *22*, 1–9. https://doi.org/10.1186/S12887-022-03436-6/TABLES/3.

13. Heijmans, B.T., Tobi, E.W., Stein, A.D., Putter, H., Blauw, G.J., Susser, E.S., Slagboom, P.E., and Lumey, L.H. (2008). Persistent epigenetic differences associated with prenatal exposure to famine in humans. Proc Natl Acad Sci U S A *105*, 17046–17049. https://doi.org/10.1073/PNAS.0806560105/ASSET/E45FA062-D76D-424C-9EBE-A06956CB0B4C/ASSETS/GRAPHIC/ZPQ9990854020001.JPEG.
14. Upadhyay, S.K., Agarwal, K.N., and Agarwal, D.K. (1989). Influence of malnutrition on social maturity, visual motor coordination & memory in rural school children. Indian J Med Res *90*, 320–327.
15. Chopra, J.S., and Sharma, A. (1992). Protein energy malnutrition and the nervous system. J Neurol Sci *110*, 8–20. https://doi.org/10.1016/0022-510X(92)90003-4.
16. Stoch, M.B., Moodie, A.D., and Bradshaw, D. (1982). Psychosocial Outcome and CT Findings after Gross Undernourishment during Infancy: a 20-year Developmental Study. Dev Med Child Neurol *24*, 419–436. https://doi.org/10.1111/J.1469-8749.1982.TB13647.X.
17. Kar, B.R., Rao, S.L., and Chandramouli, B.A. (2008). Cognitive development in children with chronic protein energy malnutrition. Behavioral and Brain Functions *4*, 1–12. https://doi.org/10.1186/1744-9081-4-31/TABLES/3.
18. Victora, C.G., Adair, L., Fall, C., Hallal, P.C., Martorell, R., Richter, L., and Sachdev, H.S. (2008). Maternal and child undernutrition: consequences for adult health and human capital. The Lancet *371*, 340–357. https://doi.org/10.1016/S0140-6736(07)61692-4/ATTACHMENT/B220BF22-B4C5-4C79-8345-C6091D8A67AC/MMC10.PDF.
19. Chattopadhyay, P.S., Gupta, S.K., Chattopadhyay, R., Kundu, P.K., and Chakraborti, R. (1995). Malnutrition-Related Diabetes Mellitus (MRDM), Not Diabetes-Related Malnutrition: A report on genuine MRDM. Diabetes Care *18*, 276–277. https://doi.org/10.2337/DIACARE.18.2.276.
20. TRIPATHY, B.B., and KAR, B.C. (1965). Observations on Clinical Patterns of Diabetes Mellitus in India. Diabetes *14*, 404–412. https://doi.org/10.2337/DIAB.14.7.404.
21. Hugh-Jones, P. (1955). DIABETES IN JAMAICA. The Lancet *266*, 891–897. https://doi.org/10.1016/S0140-6736(55)92530-7.
22. Taylor, A.K., Cao, W., Vora, K.P., De La Cruz, J., Shieh, W.J., Zaki, S.R., Katz, J.M., Sambhara, S., and Gangappa, S. (2013). Protein energy malnutrition decreases immunity and increases susceptibility to influenza infection in mice. J Infect Dis *207*, 501–510. https://doi.org/10.1093/infdis/jis527.
23. Chatraw, J.H., Wherry, E.J., Ahmed, R., and Kapasi, Z.F. (2008). Diminished primary CD8 T cell response to viral infection during protein energy malnutrition in mice is due to changes in microenvironment and low numbers of viral-specific CD8 T cell precursors. J Nutr *138*, 806–812.
24. Chandra, R.K. (1979). Nutritional deficiency and susceptibility to infection. Bull World Health Organ *57*, 167.
25. Hashimoto, T., Perlot, T., Rehman, A., Trichereau, J., Ishiguro, H., Paolino, M., Sigl, V., Hanada, T., Hanada, R., Lipinski, S., et al. (2012). ACE2 links amino acid malnutrition to microbial ecology and intestinal inflammation. Nature *487*, 477–481. https://doi.org/10.1038/nature11228.

894 26. Guiraldes, E., and Hamilton, J.R. (1981). Effect of chronic malnutrition on intestinal
895 structure, epithelial renewal, and enzymes in suckling rats. Pediatr Res *15*, 930–934.
896 https://doi.org/10.1203/00006450-198106000-00010.
897 27. Butzner, J.D., Butler, D.G., Miniats, O.P., and Hamilton, J.R. (1985). Impact of Chronic
898 Protein-Calorie Malnutrition on Small Intestinal Repair after Acute Viral Enteritis: A
899 Study in Gnotobiotic Piglets. Pediatric Research 1985 19:5 *19*, 476–481.
900 https://doi.org/10.1203/00006450-198505000-00014.
901 28. Lauer, J., Ghosh, S., Ausman, L., Webb, P., Bashaasha, B., Agaba, E.,
902 Turyashemererwa, F., Tran, H., Gewirtz, A., Erhardt, J., et al. (2020). Markers of
903 Environmental Enteric Dysfunction Are Associated with Poor Growth and Iron Status
904 in Rural Ugandan infants. Curr Dev Nutr *4*, nzaa053_064.
905 https://doi.org/10.1093/CDN/NZAA053_064.
906 29. Syed, S., Iqbal, N.T., Sadiq, K., Ma, J.Z., Akhund, T., Xin, W., Moore, S.R., Liu, E.,
907 Qureshi, S., Gosselin, K., et al. (2018). Serum anti-flagellin and anti-lipopolysaccharide
908 immunoglobulins as predictors of linear growth faltering in Pakistani infants at risk for
909 environmental enteric dysfunction. PLoS One *13*, e0193768.
910 https://doi.org/10.1371/JOURNAL.PONE.0193768.
911 30. Phiri, T.N., Mutasa, K., Rukobo, S., Govha, M., Mushayanembwa, P., Mwakamui, S.,
912 Haider, T., Zyambo, K., Dumbura, C., Tome, J., et al. (2023). Severe acute malnutrition
913 promotes bacterial binding over proinflammatory cytokine secretion by circulating
914 innate immune cells. Sci Adv *9*.
915 https://doi.org/10.1126/SCIADV.ADH2284/SUPPL_FILE/SCIADV.ADH2284_SM.PDF.
916 31. Iyer, S.S., Chatraw, J.H., Tan, W.G., Wherry, E.J., Becker, T.C., Ahmed, R., and Kapasi,
917 Z.F. (2012). Protein energy malnutrition impairs homeostatic proliferation of memory
918 CD8 T cells. J Immunol *188*, 77–84. https://doi.org/10.4049/jimmunol.1004027.
919 32. Pan, W.H., Sommer, F., Falk-Paulsen, M., Ulas, T., Best, P., Fazio, A., Kachroo, P.,
920 Luzius, A., Jentzsch, M., Rehman, A., et al. (2018). Exposure to the gut microbiota
921 drives distinct methylome and transcriptome changes in intestinal epithelial cells
922 during postnatal development. Genome Med *10*, 27. https://doi.org/10.1186/s13073-
923 018-0534-5.
924 33. McGee, D.W., and McMurray, D.N. (1988). The effect of protein malnutrition on the
925 IgA immune response in mice. Immunology *63*, 25–29.
926 34. Fazio, A., Bordoni, D., Kuiper, J.W.P., Weber-Stiehl, S., Stengel, S.T., Arnold, P.,
927 Ellinghaus, D., Ito, G., Tran, F., Messner, B., et al. (2022). DNA methyltransferase 3A
928 controls intestinal epithelial barrier function and regeneration in the colon. Nat
929 Commun *13*. https://doi.org/10.1038/s41467-022-33844-2.
930 35. Gizard, F., Amant, C., Barbier, O., Bellosta, S., Robillard, R., Percevault, F., Sevestre, H.,
931 Krimpenfort, P., Corsini, A., Rochette, J., et al. (2005). PPAR alpha inhibits vascular
932 smooth muscle cell proliferation underlying intimal hyperplasia by inducing the tumor
933 suppressor p16INK4a. J Clin Invest *115*, 3228–3238.
934 https://doi.org/10.1172/JCI22756.
935 36. Daniel, B., Nagy, G., Czimmerer, Z., Horvath, A., Hammers, D.W., Cuaranta-Monroy, I.,
936 Poliska, S., Tzerpos, P., Kolostyak, Z., Hays, T.T., et al. (2018). The Nuclear Receptor
937 PPARγ Controls Progressive Macrophage Polarization as a Ligand-Insensitive
938 Epigenomic Ratchet of Transcriptional Memory. Immunity *49*, 615-626.e6.
939 https://doi.org/10.1016/J.IMMUNI.2018.09.005.

940 37. Mishra, N., Aden, K., Blase, J.I., Baran, N., Bordoni, D., Tran, F., Conrad, C., Avalos, D.,
941 Jaeckel, C., Scherer, M., et al. (2022). Longitudinal multi-omics analysis identifies early
942 blood-based predictors of anti-TNF therapy response in inflammatory bowel disease.
943 Genome Med *14*. https://doi.org/10.1186/S13073-022-01112-Z.
944 38. Wang, D., Day, E.A., Townsend, L.K., Djordjevic, D., Jørgensen, S.B., and Steinberg,
945 G.R. (2021). GDF15: emerging biology and therapeutic applications for obesity and
946 cardiometabolic disease. Nature Reviews Endocrinology 2021 17:10 *17*, 592–607.
947 https://doi.org/10.1038/s41574-021-00529-7.
948 39. Patel, S., Alvarez-Guaita, A., Melvin, A., Rimmington, D., Dattilo, A., Miedzybrodzka,
949 E.L., Cimino, I., Maurin, A.C., Roberts, G.P., Meek, C.L., et al. (2019). GDF15 Provides
950 an Endocrine Signal of Nutritional Stress in Mice and Humans. Cell Metab *29*, 707-
951 718.e8. https://doi.org/10.1016/J.CMET.2018.12.016/ATTACHMENT/0A532AF4-
952 416C-4CD4-BFB9-C8F898B06E4E/MMC2.PDF.
953 40. Groarke, J.D., Crawford, J., Collins, S.M., Lubaczewski, S., Roeland, E.J., Naito, T.,
954 Hendifar, A.E., Fallon, M., Takayama, K., Asmis, T., et al. (2024). Ponsegromab for the
955 Treatment of Cancer Cachexia. N Engl J Med.
956 https://doi.org/10.1056/NEJMOA2409515.
957 41. Bona, M., Medeiros, P.H., Santos, A.K., Freitas, T., Prata, M., Veras, H., Amaral, M.,
958 Oliveira, D., Havt, A., and Lima, A.Â. (2019). Virulence-related genes are associated
959 with clinical and nutritional outcomes of Shigella/Enteroinvasive Escherichia coli
960 pathotype infection in children from Brazilian semiarid region: A community case-
961 control study. Int J Med Microbiol *309*, 151–158.
962 https://doi.org/10.1016/J.IJMM.2019.01.003.
963 42. Gazi, M.A., Alam, M.A., Fahim, S.M., Wahid, B.Z., Khan, S.S., Islam, M.O., Hasan,
964 M.M., Hasan, S.M.T., Das, S., Mahfuz, M., et al. (2022). Infection With Escherichia Coli
965 Pathotypes Is Associated With Biomarkers of Gut Enteropathy and Nutritional Status
966 Among Malnourished Children in Bangladesh. Front Cell Infect Microbiol *12*.
967 https://doi.org/10.3389/FCIMB.2022.901324.
968 43. Rakoff-Nahoum, S., Paglino, J., Eslami-Varzaneh, F., Edberg, S., and Medzhitov, R.
969 (2004). Recognition of commensal microflora by toll-like receptors is required for
970 intestinal homeostasis. Cell *118*, 229–241. https://doi.org/10.1016/j.cell.2004.07.002
971 S0092867404006610 [pii].
972 44. Quaranta, A., Revol-Cavalier, J., and Wheelock, C.E. (2022). The octadecanoids: an
973 emerging class of lipid mediators. Biochem Soc Trans *50*, 1569–1582.
974 https://doi.org/10.1042/BST20210644.
975 45. Levan, S.R., Stamnes, K.A., Lin, D.L., Panzer, A.R., Fukui, E., McCauley, K., Fujimura,
976 K.E., McKean, M., Ownby, D.R., Zoratti, E.M., et al. (2019). Elevated faecal 12,13-
977 diHOME concentration in neonates at high risk for asthma is produced by gut bacteria
978 and impedes immune tolerance. Nat Microbiol *4*, 1851–1861.
979 https://doi.org/10.1038/S41564-019-0498-2.
980 46. Cunha, M.C.R., Lima, F. da S., Vinolo, M.A.R., Hastreiter, A., Curi, R., Borelli, P., and
981 Fock, R.A. (2013). Protein Malnutrition Induces Bone Marrow Mesenchymal Stem
982 Cells Commitment to Adipogenic Differentiation Leading to Hematopoietic Failure.
983 PLoS One *8*, e58872. https://doi.org/10.1371/JOURNAL.PONE.0058872.
984 47. Varnat, F., Heggeler, B.B. Ten, Grisel, P., Boucard, N., Corthésy-Theulaz, I., Wahli, W.,
985 and Desvergne, B. (2006). PPARβ/δ Regulates Paneth Cell Differentiation Via

986 Controlling the Hedgehog Signaling Pathway. Gastroenterology *131*, 538–553.
987 https://doi.org/10.1053/J.GASTRO.2006.05.004.
988 48. Aguilar-Recarte, D., Barroso, E., Gumà, A., Pizarro-Delgado, J., Peña, L., Ruart, M.,
989 Palomer, X., Wahli, W., and Vázquez-Carrera, M. (2021). GDF15 mediates the
990 metabolic effects of PPARβ/δ by activating AMPK. Cell Rep *36*.
991 https://doi.org/10.1016/J.CELREP.2021.109501.
992 49. Wan, Y., and Fu, J. (2023). GDF15 as a key disease target and biomarker: linking
993 chronic lung diseases and ageing. Molecular and Cellular Biochemistry 2023 479:3
994 *479*, 453–466. https://doi.org/10.1007/S11010-023-04743-X.
995 50. Sato, T., Stange, D.E., Ferrante, M., Vries, R.G.J., Van Es, J.H., Van Den Brink, S., Van
996 Houdt, W.J., Pronk, A., Van Gorp, J., Siersema, P.D., et al. (2011). Long-term
997 expansion of epithelial organoids from human colon, adenoma, adenocarcinoma, and
998 Barrett's epithelium. Gastroenterology *141*, 1762–1772.
999 https://doi.org/10.1053/J.GASTRO.2011.07.050.
1000 51. Olsen, O.E., Skjærvik, A., Størdal, B.F., Sundan, A., and Holien, T. (2017). TGF-β
1001 contamination of purified recombinant GDF15. PLoS One *12*, e0187349.
1002 https://doi.org/10.1371/JOURNAL.PONE.0187349.
1003 52. Mostafa, I., Nahar, N.N., Islam, M.M., Huq, S., Mustafa, M., Barratt, M., Gordon, J.I.,
1004 and Ahmed, T. (2020). Proof-of-concept study of the efficacy of a microbiota-directed
1005 complementary food formulation (MDCF) for treating moderate acute malnutrition.
1006 BMC Public Health *20*, 242. https://doi.org/10.1186/s12889-020-8330-8.
1007 53. Reyes, A., Blanton, L. V, Cao, S., Zhao, G., Manary, M., Trehan, I., Smith, M.I., Wang,
1008 D., Virgin, H.W., Rohwer, F., et al. (2015). Gut DNA viromes of Malawian twins
1009 discordant for severe acute malnutrition. Proc Natl Acad Sci U S A *112*, 11941–11946.
1010 https://doi.org/10.1073/pnas.1514285112.
1011 54. Schwarzer, M., Makki, K., Storelli, G., Machuca-Gayet, I., Srutkova, D., Hermanova, P.,
1012 Martino, M.E., Balmand, S., Hudcovic, T., Heddi, A., et al. (2016). Lactobacillus
1013 plantarum strain maintains growth of infant mice during chronic undernutrition.
1014 Science (1979) *351*, 854–857. https://doi.org/10.1126/science.aad8588.
1015 55. Storelli, G., Defaye, A., Erkosar, B., Hols, P., Royet, J., and Leulier, F. (2011).
1016 Lactobacillus plantarum promotes Drosophila systemic growth by modulating
1017 hormonal signals through TOR-dependent nutrient sensing. Cell Metab *14*, 403–414.
1018 https://doi.org/10.1016/j.cmet.2011.07.012.
1019 56. Kau, A.L., Planer, J.D., Liu, J., Rao, S., Yatsunenko, T., Trehan, I., Manary, M.J., Liu, T.C.,
1020 Stappenbeck, T.S., Maleta, K.M., et al. (2015). Functional characterization of IgA-
1021 targeted bacterial taxa from undernourished Malawian children that produce diet-
1022 dependent enteropathy. Sci Transl Med *7*, 276ra24.
1023 https://doi.org/10.1126/scitranslmed.aaa4877.
1024 57. Charbonneau, M.R., O'Donnell, D., Blanton, L. V, Totten, S.M., Davis, J.C., Barratt,
1025 M.J., Cheng, J., Guruge, J., Talcott, M., Bain, J.R., et al. (2016). Sialylated Milk
1026 Oligosaccharides Promote Microbiota-Dependent Growth in Models of Infant
1027 Undernutrition. Cell *164*, 859–871. https://doi.org/10.1016/j.cell.2016.01.024.
1028 58. Hartman, S.J., Hibberd, M.C., Mostafa, I., Naila, N.N., Islam, Md.M., Zaman, M.U.,
1029 Huq, S., Mahfuz, M., Islam, Md.T., Mukherji, K., et al. (2024). A microbiome-directed
1030 therapeutic food for children recovering from severe acute malnutrition. Sci Transl
1031 Med *16*. https://doi.org/10.1126/SCITRANSLMED.ADN2366.

1032 59. Chama, M., Amadi, B.C., Chandwe, K., Zyambo, K., Besa, E., Shaikh, N., Ndao, I.M.,
1033 Tarr, P.I., Storer, C., Head, R., et al. (2019). Transcriptomic analysis of enteropathy in
1034 Zambian children with severe acute malnutrition. EBioMedicine *45*, 456–463.
1035 https://doi.org/10.1016/J.EBIOM.2019.06.015.
1036 60. Schulze, K. V., Swaminathan, S., Howell, S., Jajoo, A., Lie, N.C., Brown, O., Sadat, R.,
1037 Hall, N., Zhao, L., Marshall, K., et al. (2019). Edematous severe acute malnutrition is
1038 characterized by hypomethylation of DNA. Nature Communications 2019 10:1 *10*, 1–
1039 13. https://doi.org/10.1038/s41467-019-13433-6.
1040 61. Blanton, L. V, Charbonneau, M.R., Salih, T., Barratt, M.J., Venkatesh, S., Ilkaveya, O.,
1041 Subramanian, S., Manary, M.J., Trehan, I., Jorgensen, J.M., et al. (2016). Gut bacteria
1042 that prevent growth impairments transmitted by microbiota from malnourished
1043 children. Science (1979) *351*. https://doi.org/10.1126/science.aad3311.
1044 62. Mulenga, C., Sviben, S., Chandwe, K., Amadi, B., Kayamba, V., Fitzpatrick, J.A.J.,
1045 Mudenda, V., and Kelly, P. (2022). Epithelial Abnormalities in the Small Intestine of
1046 Zambian Children With Stunting. Front Med (Lausanne) *9*.
1047 https://doi.org/10.3389/FMED.2022.849677.
1048 63. Kelly, P., Amadi, B., Chandwe, K., Besa, E., Zyambo, K., Chama, M., Tarr, P.I., Shaikh,
1049 N., Ndao, I.M., Storer, C., et al. (2021). Gene expression profiles compared in
1050 environmental and malnutrition enteropathy in Zambian children and adults.
1051 EBioMedicine *70*. https://doi.org/10.1016/j.ebiom.2021.103509.
1052 64. Howell, K.J., Kraiczy, J., Nayak, K.M., Gasparetto, M., Ross, A., Lee, C., Mak, T.N., Koo,
1053 B.K., Kumar, N., Lawley, T., et al. (2018). DNA Methylation and Transcription Patterns
1054 in Intestinal Epithelial Cells From Pediatric Patients With Inflammatory Bowel
1055 Diseases Differentiate Disease Subtypes and Associate With Outcome.
1056 Gastroenterology *154*, 585–598. https://doi.org/10.1053/J.GASTRO.2017.10.007.
1057 65. Kraiczy, J., Nayak, K.M., Howell, K.J., Ross, A., Forbester, J., Salvestrini, C., Mustata, R.,
1058 Perkins, S., Andersson-Rolf, A., Leenen, E., et al. (2019). DNA methylation defines
1059 regional identity of human intestinal epithelial organoids and undergoes dynamic
1060 changes during development. Gut *68*, 49–61. https://doi.org/10.1136/GUTJNL-2017-
1061 314817.
1062 66. Li, H.J., Ray, S.K., Pan, N., Haigh, J., Fritzsch, B., and Leiter, A.B. (2019). Intestinal
1063 Neurod1 expression impairs paneth cell differentiation and promotes
1064 enteroendocrine lineage specification. Sci Rep *9*. https://doi.org/10.1038/S41598-
1065 019-55292-7.
1066 67. Gross, B., Pawlak, M., Lefebvre, P., and Staels, B. (2017). PPARs in obesity-induced
1067 T2DM, dyslipidaemia and NAFLD. Nat Rev Endocrinol *13*, 36–49.
1068 https://doi.org/10.1038/NRENDO.2016.135.
1069 68. Wang, D., Townsend, L.K., DesOrmeaux, G.J., Frangos, S.M., Batchuluun, B., Dumont,
1070 L., Kuhre, R.E., Ahmadi, E., Hu, S., Rebalka, I.A., et al. (2023). GDF15 promotes weight
1071 loss by enhancing energy expenditure in muscle. Nature *619*, 143–150.
1072 https://doi.org/10.1038/S41586-023-06249-4.
1073 69. Coll, A.P., Chen, M., Taskar, P., Rimmington, D., Patel, S., Tadross, J.A., Cimino, I.,
1074 Yang, M., Welsh, P., Virtue, S., et al. (2020). GDF15 mediates the effects of metformin
1075 on body weight and energy balance. Nature *578*, 444–448.
1076 https://doi.org/10.1038/S41586-019-1911-Y.

70. Sommer, F., Anderson, J.M., Bharti, R., Raes, J., and Rosenstiel, P. (2017). The resilience of the intestinal microbiota influences health and disease. Nat Rev Microbiol. https://doi.org/10.1038/nrmicro.2017.58.
71. Bäckhed, F., Ding, H., Wang, T., Hooper, L. V, Koh, G.Y., Nagy, A., Semenkovich, C.F., and Gordon, J.I. (2004). The gut microbiota as an environmental factor that regulates fat storage. Proc Natl Acad Sci U S A *101*, 15718–15723. https://doi.org/10.1073/pnas.0407076101.
72. Turnbaugh, P.J., Ley, R.E., Mahowald, M.A., Magrini, V., Mardis, E.R., and Gordon, J.I. (2006). An obesity-associated gut microbiome with increased capacity for energy harvest. Nature *444*, 1027–1031. https://doi.org/nature05414 [pii] 10.1038/nature05414.
73. Itoh, T., Fairall, L., Amin, K., Inaba, Y., Szanto, A., Balint, B.L., Nagy, L., Yamamoto, K., and Schwabe, J.W.R. (2008). Structural basis for the activation of PPARγ by oxidized fatty acids. Nature Structural & Molecular Biology 2008 15:9 *15*, 924–931. https://doi.org/10.1038/nsmb.1474.
74. Levan, S.R., Stamnes, K.A., Lin, D.L., Panzer, A.R., Fukui, E., McCauley, K., Fujimura, K.E., McKean, M., Ownby, D.R., Zoratti, E.M., et al. (2019). Elevated faecal 12,13-diHOME concentration in neonates at high risk for asthma is produced by gut bacteria and impedes immune tolerance. Nature Microbiology 2019 4:11 *4*, 1851–1861. https://doi.org/10.1038/s41564-019-0498-2.
75. Nagy, L., Tontonoz, P., Alvarez, J.G.A., Chen, H., and Evans, R.M. (1998). Oxidized LDL regulates macrophage gene expression through ligand activation of PPARgamma. Cell *93*, 229–240. https://doi.org/10.1016/S0092-8674(00)81574-3.
76. Kincaid, J.W.R., Rimmington, D., Tadross, J.A., Cimino, I., Zvetkova, I., Kaser, A., Richards, P., Patel, S., O'Rahilly, S., and Coll, A.P. (2024). The gastrointestinal tract is a major source of the acute metformin-stimulated rise in GDF15. Sci Rep *14*. https://doi.org/10.1038/S41598-024-51866-2.
77. Suriben, R., Chen, M., Higbee, J., Oeffinger, J., Ventura, R., Li, B., Mondal, K., Gao, Z., Ayupova, D., Taskar, P., et al. (2020). Antibody-mediated inhibition of GDF15–GFRAL activity reverses cancer cachexia in mice. Nature Medicine 2020 26:8 *26*, 1264–1270. https://doi.org/10.1038/s41591-020-0945-x.
78. Groarke, J.D., Crawford, J., Collins, S.M., Lubaczewski, S.L., Breen, D.M., Harrington, M.A., Jacobs, I., Qiu, R., Revkin, J., Rossulek, M.I., et al. (2024). Phase 2 study of the efficacy and safety of ponsegromab in patients with cancer cachexia: PROACC-1 study design. J Cachexia Sarcopenia Muscle *15*, 1054–1061. https://doi.org/10.1002/JCSM.13435.
79. Badaloo, A. V., Forrester, T., Reid, M., and Jahoor, F. (2006). Lipid kinetic differences between children with kwashiorkor and those with marasmus. Am J Clin Nutr *83*, 1283–1288. https://doi.org/10.1093/AJCN/83.6.1283.
80. Bartz, S., Mody, A., Hornik, C., Bain, J., Muehlbauer, M., Kiyimba, T., Kiboneka, E., Stevens, R., Bartlett, J., St Peter, J. V., et al. (2014). Severe Acute Malnutrition in Childhood: Hormonal and Metabolic Status at Presentation, Response to Treatment, and Predictors of Mortality. J Clin Endocrinol Metab *99*, 2128–2137. https://doi.org/10.1210/JC.2013-4018.
81. Mahmud, I., Kabir, M., Haque, R., and Garrett, T.J. (2019). Decoding the Metabolome and Lipidome of Child Malnutrition by Mass Spectrometric Techniques: Present Status

and Future Perspectives. Anal Chem *91*, 14784. https://doi.org/10.1021/ACS.ANALCHEM.9B03338.

82. Oxidation of free fatty acids of plasma in infants with protein-calorie malnutrition | South African Medical Journal https://journals.co.za/doi/10.10520/AJA20785135_34805.

83. Sawada, M., Takahashi, K., Sawada, S., and Midorikawa, O. (1991). Selective killing of Paneth cells by intravenous administration of dithizone in rats. Int J Exp Pathol *72*, 407.

84. Yilmaz, O.H., Katajisto, P., Lamming, D.W., Gultekin, Y., Bauer-Rowe, K.E., Sengupta, S., Birsoy, K., Dursun, A., Yilmaz, V.O., Selig, M., et al. (2012). mTORC1 in the Paneth cell niche couples intestinal stem-cell function to calorie intake. Nature *486*, 490–495. https://doi.org/10.1038/nature11163.

85. Schmitt, M., Schewe, M., Sacchetti, A., Feijtel, D., van de Geer, W.S., Teeuwssen, M., Sleddens, H.F., Joosten, R., van Royen, M.E., van de Werken, H.J.G., et al. (2018). Paneth Cells Respond to Inflammation and Contribute to Tissue Regeneration by Acquiring Stem-like Features through SCF/c-Kit Signaling. Cell Rep *24*, 2312-2328.e7. https://doi.org/10.1016/J.CELREP.2018.07.085.

86. Thurstans, S., Opondo, C., Seal, A., Wells, J., Khara, T., Dolan, C., Briend, A., Myatt, M., Garenne, M., Sear, R., et al. (2020). Boys are more likely to be undernourished than girls: a systematic review and meta-analysis of sex differences in undernutrition. BMJ Glob Health *5*, e004030. https://doi.org/10.1136/BMJGH-2020-004030.

87. WHO (2016). WHO recommendations on antenatal care. WHO Library Cataloguing, 172.

88. Agus, A., Planchais, J., and Sokol, H. (2018). Gut Microbiota Regulation of Tryptophan Metabolism in Health and Disease. Cell Host Microbe *23*, 716–724. https://doi.org/10.1016/J.CHOM.2018.05.003.

89. Cadwell, K., Liu, J.Y., Brown, S.L., Miyoshi, H., Loh, J., Lennerz, J.K., Kishi, C., Kc, W., Carrero, J.A., Hunt, S., et al. (2008). A key role for autophagy and the autophagy gene Atg16l1 in mouse and human intestinal Paneth cells. Nature *456*, 259–263. https://doi.org/10.1038/NATURE07416.

90. Adolph, T.E., Tomczak, M.F., Niederreiter, L., Ko, H.J., Böck, J., Martinez-Naves, E., Glickman, J.N., Tschurtschenthaler, M., Hartwig, J., Hosomi, S., et al. (2013). Paneth cells as a site of origin for intestinal inflammation. Nature *503*, 272–276. https://doi.org/10.1038/NATURE12599.

91. Sato, T., Vries, R.G., Snippert, H.J., van de Wetering, M., Barker, N., Stange, D.E., van Es, J.H., Abo, A., Kujala, P., Peters, P.J., et al. (2009). Single Lgr5 stem cells build crypt-villus structures in vitro without a mesenchymal niche. Nature *459*, 262–265. https://doi.org/10.1038/nature07935.

92. nf-core/rnaseq: nf-core/rnaseq v3.14.0 - Hassium Honey Badger https://doi.org/10.5281/ZENODO.10471647.

93. Dobin, A., Davis, C.A., Schlesinger, F., Drenkow, J., Zaleski, C., Jha, S., Batut, P., Chaisson, M., and Gingeras, T.R. (2013). STAR: ultrafast universal RNA-seq aligner. Bioinformatics *29*, 15–21. https://doi.org/10.1093/BIOINFORMATICS/BTS635.

94. Liao, Y., Smyth, G.K., and Shi, W. (2014). featureCounts: an efficient general purpose program for assigning sequence reads to genomic features. Bioinformatics *30*, 923–930. https://doi.org/10.1093/BIOINFORMATICS/BTT656.

1169 95. Love, M.I., Huber, W., and Anders, S. (2014). Moderated estimation of fold change
1170 and dispersion for RNA-seq data with DESeq2. Genome Biol *15*.
1171 https://doi.org/10.1186/S13059-014-0550-8.
1172 96. Alexa, A., Rahnenfuhrer, J., and Lengauer, T. (2006). Improved scoring of functional
1173 groups from gene expression data by decorrelating GO graph structure.
1174 Bioinformatics *22*, 1600–1607. https://doi.org/10.1093/bioinformatics/btl140.
1175 97. Sheffield, N.C., and Bock, C. (2016). LOLA: enrichment analysis for genomic region
1176 sets and regulatory elements in R and Bioconductor. Bioinformatics *32*, 587–589.
1177 https://doi.org/10.1093/BIOINFORMATICS/BTV612.
1178 98. Hao, Y., Hao, S., Andersen-Nissen, E., Mauck, W.M., Zheng, S., Butler, A., Lee, M.J.,
1179 Wilk, A.J., Darby, C., Zager, M., et al. (2021). Integrated analysis of multimodal single-
1180 cell data. Cell *184*, 3573-3587.e29. https://doi.org/10.1016/J.CELL.2021.04.048.
1181 99. Hafemeister, C., and Satija, R. (2019). Normalization and variance stabilization of
1182 single-cell RNA-seq data using regularized negative binomial regression. Genome Biol
1183 *20*. https://doi.org/10.1186/S13059-019-1874-1.
1184 100. Yu, G., Wang, L.G., Han, Y., and He, Q.Y. (2012). clusterProfiler: an R package for
1185 comparing biological themes among gene clusters. OMICS *16*, 284–287.
1186 https://doi.org/10.1089/OMI.2011.0118.
1187 101. Assenov, Y., Müller, F., Lutsik, P., Walter, J., Lengauer, T., and Bock, C. (2014).
1188 Comprehensive analysis of DNA methylation data with RnBeads. Nat Methods *11*,
1189 1138–1140. https://doi.org/10.1038/NMETH.3115.
1190 102. Bernardes, J.P., Mishra, N., Tran, F., Bahmer, T., Best, L., Blase, J.I., Bordoni, D.,
1191 Franzenburg, J., Geisen, U., Josephs-Spaulding, J., et al. (2020). Longitudinal Multi-
1192 omics Analyses Identify Responses of Megakaryocytes, Erythroid Cells, and
1193 Plasmablasts as Hallmarks of Severe COVID-19. Immunity *53*, 1296-1314 e9.
1194 https://doi.org/10.1016/j.immuni.2020.11.017.
1195 103. Varga, A., Makszin, L., Bufa, A., Sipos, D., Kása, P., Pál, S., Rosenstiel, P., Sommer, F.,
1196 Kocsis, B., and Péterfi, Z. (2023). Efficacy of lyophilised bacteria-rich faecal sediment
1197 and supernatant with reduced bacterial count for treating patients with Clostridioides
1198 difficile Infection – A novel method for capsule faecal microbiota transfer. Front Cell
1199 Infect Microbiol *13*. https://doi.org/10.3389/fcimb.2023.1041384.
1200 104. Castrillón-Betancur, J.C., López-Agudelo, V.A., Sommer, N., Cleeves, S., Bernardes,
1201 J.P., Weber-Stiehl, S., Rosenstiel, P., and Sommer, F. (2023). Epithelial Dual Oxidase 2
1202 Shapes the Mucosal Microbiome and Contributes to Inflammatory Susceptibility.
1203 Antioxidants (Basel) *12*. https://doi.org/10.3390/ANTIOX12101889.
1204 105. Fadrosh, D.W., Ma, B., Gajer, P., Sengamalay, N., Ott, S., Brotman, R.M., and Ravel, J.
1205 (2014). An improved dual-indexing approach for multiplexed 16S rRNA gene
1206 sequencing on the Illumina MiSeq platform. Microbiome *2*.
1207 https://doi.org/10.1186/2049-2618-2-6.
1208 106. Caporaso, J.G., Lauber, C.L., Walters, W.A., Berg-Lyons, D., Huntley, J., Fierer, N.,
1209 Owens, S.M., Betley, J., Fraser, L., Bauer, M., et al. (2012). Ultra-high-throughput
1210 microbial community analysis on the Illumina HiSeq and MiSeq platforms. ISME J *6*,
1211 1621–1624. https://doi.org/10.1038/ismej.2012.8.
1212 107. Caporaso, J.G., Kuczynski, J., Stombaugh, J., Bittinger, K., Bushman, F.D., Costello, E.K.,
1213 Fierer, N., Pena, A.G., Goodrich, J.K., Gordon, J.I., et al. (2010). QIIME allows analysis
1214 of high-throughput community sequencing data. Nat Methods *7*, 335–336.
1215 https://doi.org/10.1038/nmeth.f.303.

108. Bolyen, E., Rideout, J.R., Dillon, M.R., Bokulich, N.A., Abnet, C.C., Al-Ghalith, G.A., Alexander, H., Alm, E.J., Arumugam, M., Asnicar, F., et al. (2019). Reproducible, interactive, scalable and extensible microbiome data science using QIIME 2. Nat Biotechnol *37*, 852–857. https://doi.org/10.1038/S41587-019-0209-9.
109. Callahan, B.J., McMurdie, P.J., Rosen, M.J., Han, A.W., Johnson, A.J.A., and Holmes, S.P. (2016). DADA2: High-resolution sample inference from Illumina amplicon data. Nat Methods *13*, 581–583. https://doi.org/10.1038/NMETH.3869.
110. Quast, C., Pruesse, E., Yilmaz, P., Gerken, J., Schweer, T., Yarza, P., Peplies, J., and Glöckner, F.O. (2013). The SILVA ribosomal RNA gene database project: improved data processing and web-based tools. Nucleic Acids Res *41*. https://doi.org/10.1093/NAR/GKS1219.
111. McMurdie, P.J., and Holmes, S. (2013). phyloseq: An R Package for Reproducible Interactive Analysis and Graphics of Microbiome Census Data. PLoS One *8*, e61217. https://doi.org/10.1371/journal.pone.0061217.
112. Blanco-Míguez, A., Beghini, F., Cumbo, F., McIver, L.J., Thompson, K.N., Zolfo, M., Manghi, P., Dubois, L., Huang, K.D., Thomas, A.M., et al. (2023). Extending and improving metagenomic taxonomic profiling with uncharacterized species using MetaPhlAn 4. Nature Biotechnology 2023 41:11 *41*, 1633–1644. https://doi.org/10.1038/s41587-023-01688-w.
113. Beghini, F., McIver, L.J., Blanco-Míguez, A., Dubois, L., Asnicar, F., Maharjan, S., Mailyan, A., Manghi, P., Scholz, M., Thomas, A.M., et al. (2021). Integrating taxonomic, functional, and strain-level profiling of diverse microbial communities with biobakery 3. Elife *10*. https://doi.org/10.7554/ELIFE.65088.
114. Dixon, P. (2003). VEGAN, a package of R functions for community ecology. Journal of Vegetation Science *14*, 927–930. https://doi.org/10.1111/j.1654-1103.2003.tb02228.x.
115. Mallick, H., Rahnavard, A., McIver, L.J., Ma, S., Zhang, Y., Nguyen, L.H., Tickle, T.L., Weingart, G., Ren, B., Schwager, E.H., et al. (2021). Multivariable association discovery in population-scale meta-omics studies. PLoS Comput Biol *17*, e1009442. https://doi.org/10.1371/journal.pcbi.1009442.
116. Mallick, H., Rahnavard, A., McIver, L.J., Ma, S., Zhang, Y., Nguyen, L.H., Tickle, T.L., Weingart, G., Ren, B., Schwager, E.H., et al. (2021). Multivariable association discovery in population-scale meta-omics studies. PLoS Comput Biol *17*, e1009442. https://doi.org/10.1371/journal.pcbi.1009442.
117. Suzek, B.E., Wang, Y., Huang, H., McGarvey, P.B., and Wu, C.H. (2015). UniRef clusters: a comprehensive and scalable alternative for improving sequence similarity searches. Bioinformatics *31*, 926–932. https://doi.org/10.1093/BIOINFORMATICS/BTU739.
118. Kaminski, J., Gibson, M.K., Franzosa, E.A., Segata, N., Dantas, G., and Huttenhower, C. (2015). High-Specificity Targeted Functional Profiling in Microbial Communities with ShortBRED. PLoS Comput Biol *11*. https://doi.org/10.1371/JOURNAL.PCBI.1004557.
119. Sillner, N., Walker, A., Harrieder, E.M., Schmitt-Kopplin, P., and Witting, M. (2019). Development and application of a HILIC UHPLC-MS method for polar fecal metabolome profiling. Journal of Chromatography B *1109*, 142–148. https://doi.org/10.1016/J.JCHROMB.2019.01.016.

120. Sillner, N., Walker, A., Koch, W., Witting, M., and Schmitt-Kopplin, P. (2018). Metformin impacts cecal bile acid profiles in mice. Journal of Chromatography B *1083*, 35–43. https://doi.org/10.1016/J.JCHROMB.2018.02.029.
121. Dührkop, K., Fleischauer, M., Ludwig, M., Aksenov, A.A., Melnik, A. V., Meusel, M., Dorrestein, P.C., Rousu, J., and Böcker, S. (2019). SIRIUS 4: a rapid tool for turning tandem mass spectra into metabolite structure information. Nature Methods 2019 16:4 *16*, 299–302. https://doi.org/10.1038/s41592-019-0344-8.

1270 **Declarations**

1271 **Funding**

1272 This work was supported by the German Research Foundation (DFG) through the
1273 Collaborative Research Centre CRC1182 “Origin and Function of Metaorganisms” (project C2,
1274 A2 and Z3), the Excellence Cluster EXS2167 “Precision Medicine in Chronic Inflammation”, the
1275 individual grant SO1141/10-1 and the Research Unit FOR5042 “miTarget - The Microbiome as
1276 a Target in Inflammatory Bowel Diseases” (projects P3, P4 and P7). RB is supported by the NIH
1277 grant DK088199. JMP received funding from the T. von Zastrow foundation and the German
1278 Federal Ministry of Education and Research (BMBF) under the project "Microbial Stargazing -
1279 Erforschung von Resilienzmechanismen von Mikroben und Menschen" (Ref. 01KX2324).

1280

1281 **Acknowledgments**

1282 The authors thank Sabine Kock, Stefanie Baumgarten, Maren Reffelmann, Vivian Wegner,
1283 Tanja Klostermeier, Dorina Ölsner, Meike Hansen, Ronja Möhring and Sophie Reiher for
1284 excellent technical assistance. We further thank Hans-Christian Behrens for providing access
1285 to the Hamamatsu NanoZoomer S60 Digital Slide Scanner, Jacob Hamm for experimental
1286 support and Robert Häsler, Louise Thingholm, Eike Wacker and David Ellinghaus for valuable
1287 input regarding the RNAseq and metagenomic analyses. We thank Anthony Coll, John Tadross
1288 and Stephen O´ Rahilly, University Cambridge for insightful critical discussions and provision
1289 of reagents.

1290

1291 **Author contributions**

1292 FS, NM, NS, FS and PR designed research. FS, NM, VL, NS, JPB, AW, FH, TG, FG, LS, AB, SK, SW,
1293 GI, FT, FS and PR performed experiments and analyzed the data. SS, JMP, RSB, PSK, JFB
1294 provided critical resources. FS, NM, VL, JPB, FS and PR prepared the figures. FS and PR
1295 obtained funding. FS, NM, VL, JPB, FH, FS and PR co-wrote the manuscript with critical input
1296 from all authors. All authors read and approved the final manuscript.

1297

1298 **Declaration of Interests**

The authors declare no competing interests.

1301 **Figures and Tables**

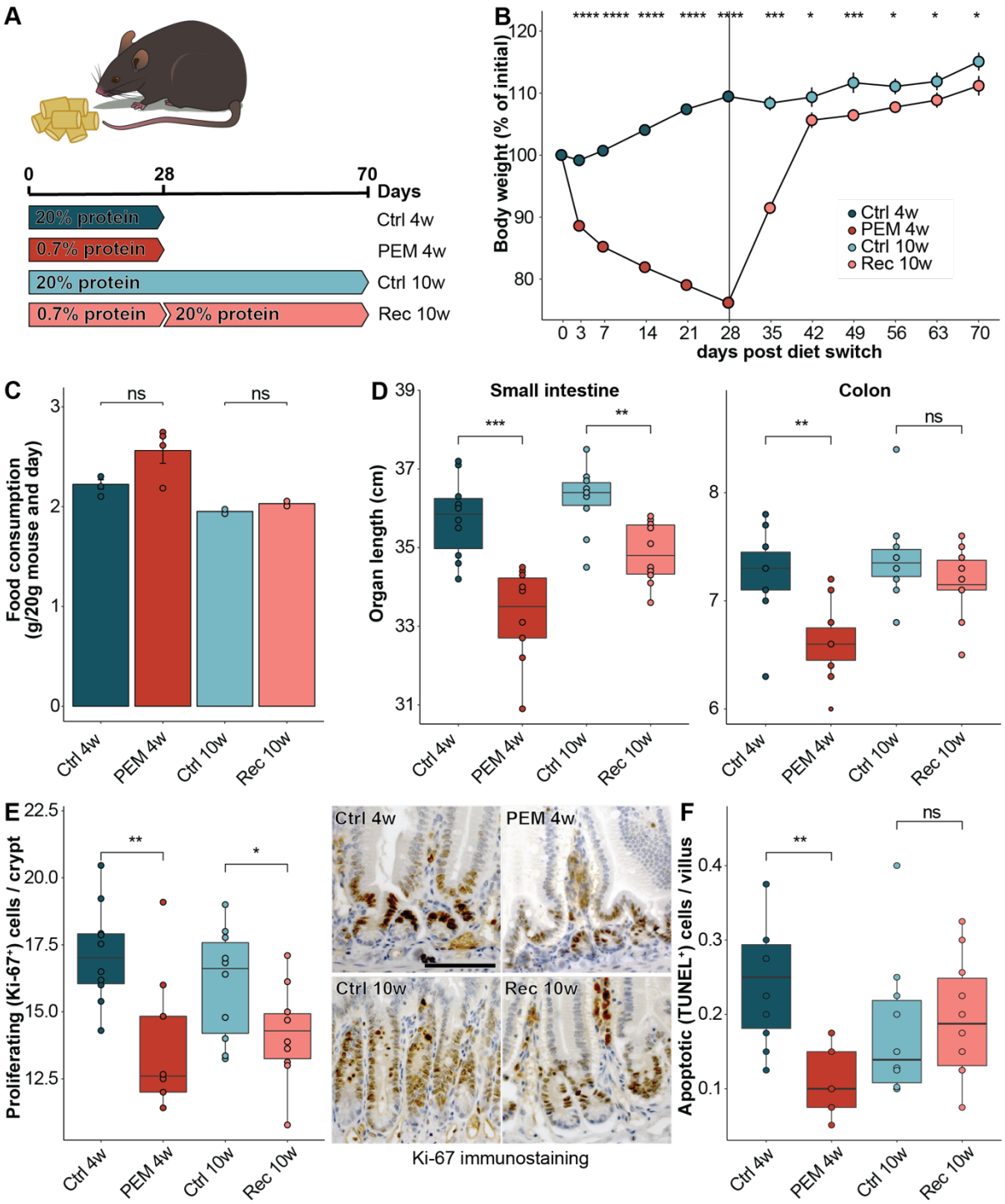

1302

1303 **Figure 1: PEM induces long-lasting changes in intestinal physiology independent of caloric**
1304 **intake. A)** Scheme of the PEM regimen in mice (n=10 mice per group). 12-week-old C57BL6
1305 mice were given either isocaloric control or protein-reduced food for 28 days to induce an
1306 acute PEM, and the PEM-mice were then switched to control diet as well for an additional 42
1307 days to monitor recovery from PEM. **B)** Body weight curve shows drastic weight loss during

1308 PEM and incomplete recovery after switch to control diet. *p < 0.05, ***p < 0.001 and ****p
1309 < 0.0001 using two-way ANOVA. **C)** Food intake of the experimental groups. ns = not
1310 significant using Mann-Whitney U test. **D)** Lengths of the small and large intestine during PEM
1311 and recovery. PEM shortened both the small and large intestine and the small intestinal
1312 length could not be restored during recovery. **p < 0.01, ***p < 0.001 and ns = not significant
1313 using Mann-Whitney U test. **E-F)** Fewer proliferating cells per crypt **(E)** and apoptotic cells per
1314 villus **(F)** in PEM mice as determined by Ki-67 immunostaining and TUNEL assay including
1315 representative images. The scale bar represents 50 µm. *p < 0.05, **p < 0.01 and ns = not
1316 significant using Mann-Whitney U test.

1317

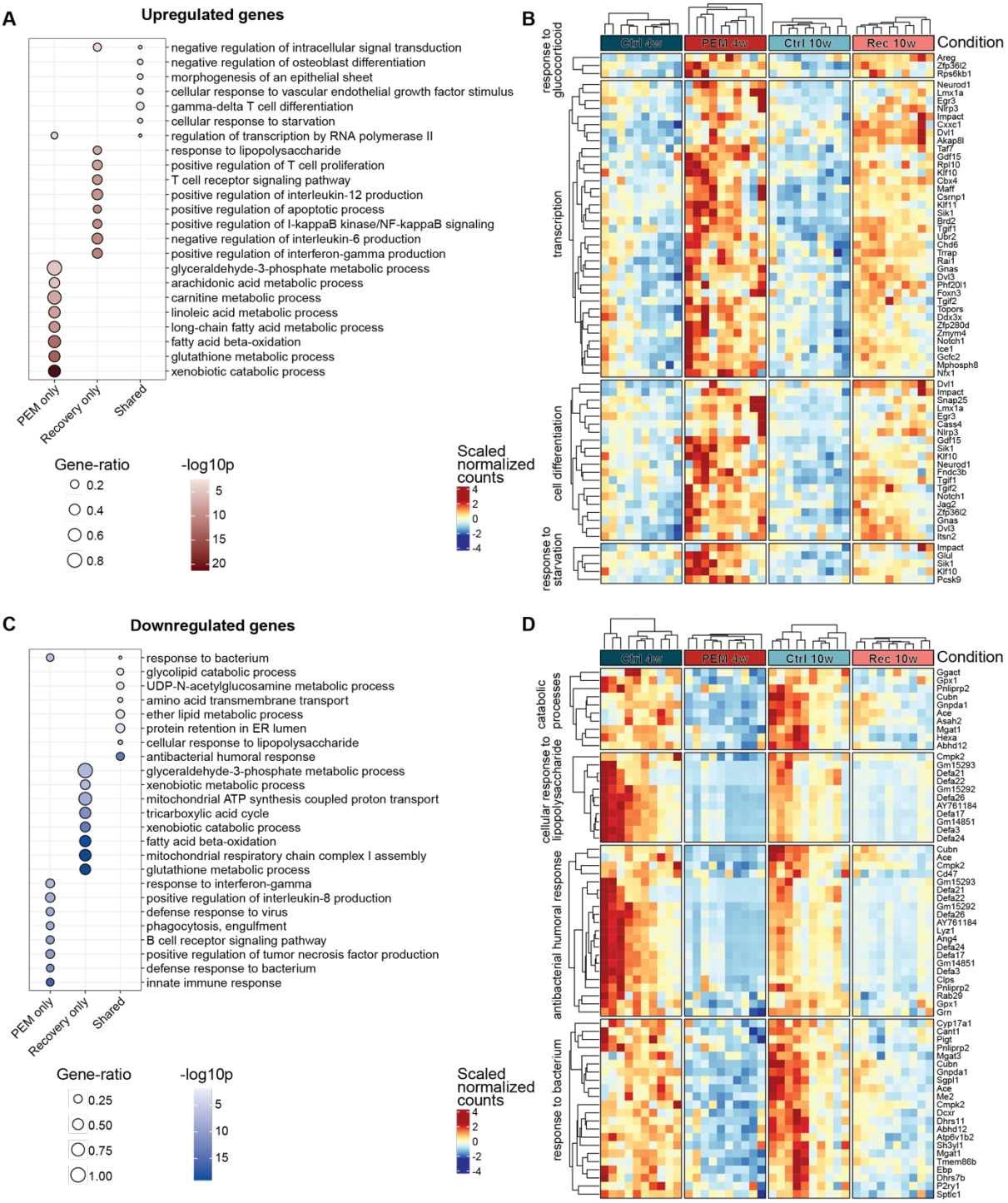

Figure 2: Transcriptome analysis of purified intestinal epithelial cells reveals lasting antimicrobial and metabolic alterations. A, C. Gene ontology (GO) terms enriched in upregulated (**A**) and downregulated (**C**) genes only at 4 weeks (PEM only), 10 weeks (Recovery only) and at both 4 and 10 weeks (Shared). Dot size is proportional to the gene ratio and color corresponds to the p-value of enrichment. Top selected terms are visualized. **B, D.** Heatmaps showing the expression of DEGs corresponding to selected GO terms enriched in upregulated

1325 (**B**) and downregulated (**D**) shared genes. Scaled normalized gene expression counts across all
1326 samples are plotted. Note that due to the GO setup, genes can belong to multiple GO
1327 categories.

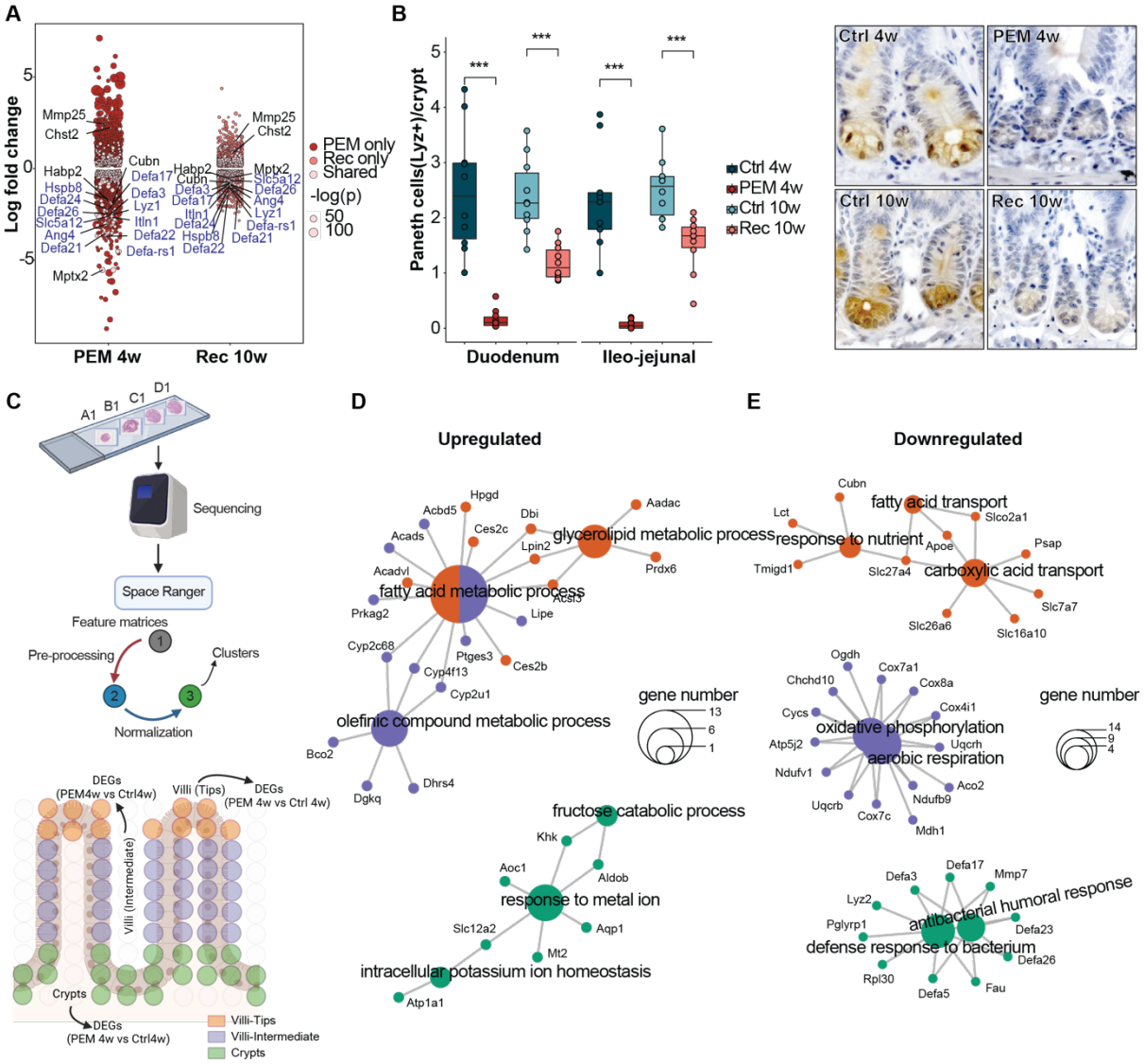

Figure 3: PEM impairs Paneth cell differentiation and leads to spatially confined gene expression changes along the crypt-villus axis. A) Log2-fold change (y axis) of differentially expressed genes (DEGs) between mice under Ctrl and PEM diet at 4 weeks and 10 weeks (x axis) with n=10 per group. Color discriminates genes that are upregulated or downregulated only at 4 weeks (PEM only), 10 weeks (Recovery only) and at both 4 and 10 weeks (Shared), and point size represents statistical significance (adjusted p value). Paneth cell related genes are highlighted in blue. **B)** Boxplots showing average number of paneth cells (Lyz+) per crypt in duodenum and ileo-jejunal regions of the small intestine of mice under Ctrl and PEM diets along with representative histological images. ***: $p < 0.001$ Ctrl_4w versus PEM_4w and Ctrl_10w versus Rec_10w using Mann-Whitney U test. **C)** Classification of spots into multiple regions: crypts represented in green, intermediate villi in purple, and villi tips in orange. Identified spots were used for DEGs analysis across PEM vs Ctrl conditions. **D-E)** Top enriched

1341 gene ontology terms of significant upregulated **(D)** and downregulated **(E)** DEGs discovered
1342 in crypts are presented. DEGs were sorted into “up” (log2foldchange > 0) and “down”
1343 (log2foldchange < 0) categories with an adjusted p-value (padj) < 0.05. Similar steps of gene
1344 ontology analysis were then applied to the Villi-Intermediate and Villi-Tip regions.

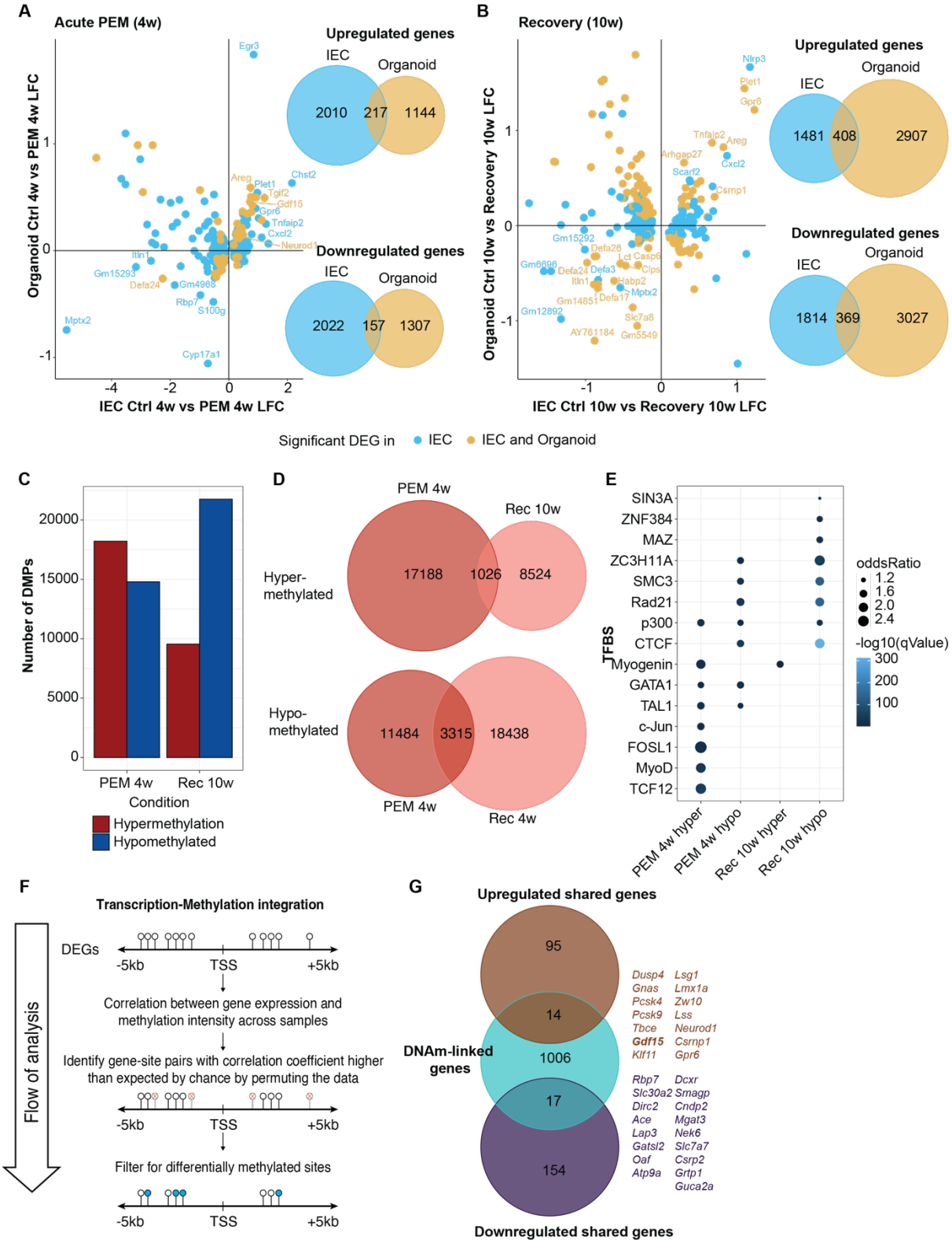

Figure 4: PEM-dependent persistent DNA methylation changes and *ex vivo* stability of gene expression changes. A-B) Comparison of transcriptional PEM effects in intestinal epithelial cells (IEC, blue) and organoids (yellow) isolated of mice from two separate dietary PEM-recovery intervention experiments during **(A)** acute PEM and **(B)** after recovery. The dot plot

1350 depicts the Log_2[fold-changes PEM_4w/10w vs Ctrl_4w/10w] whereas the Venn diagram
1351 depicts the overlap in up- and downregulated DEGs. **C)** Number of differentially (hypo- and
1352 hyper-) methylated positions (DMPs) detected by BeadCHiP array in small intestinal epithelial
1353 cells from mice during acute PEM (4 weeks) and after recovery (10 weeks) and respective
1354 controls. **D)** Shared DMPs between acute PEM (4 weeks) and recovery (10 weeks). **E)**
1355 Predicted transcription factor binding sites enriched in observed DMPs. Dot size is
1356 proportional to the odds ratio and color corresponds to the p-value of enrichment. Top
1357 selected transcription factors are visualized. **F)** Schematic depiction of gene expression - DNA
1358 methylation integration analysis. Spearman's rank correlation coefficient between the
1359 methylation intensity and gene expression values was calculated between the DMPs located
1360 within a range of 5kb before or after the transcription start site of the respective DEG. **G)**
1361 Venn Diagram depicting the overlaps between shared DEGs between PEM_4w and Rec_10w
1362 and DEGs correlated with their nearby DMPs, identifying 31 candidate DEGs linked with DMPs
1363 including GDF15 that has been linked to body mass regulation.

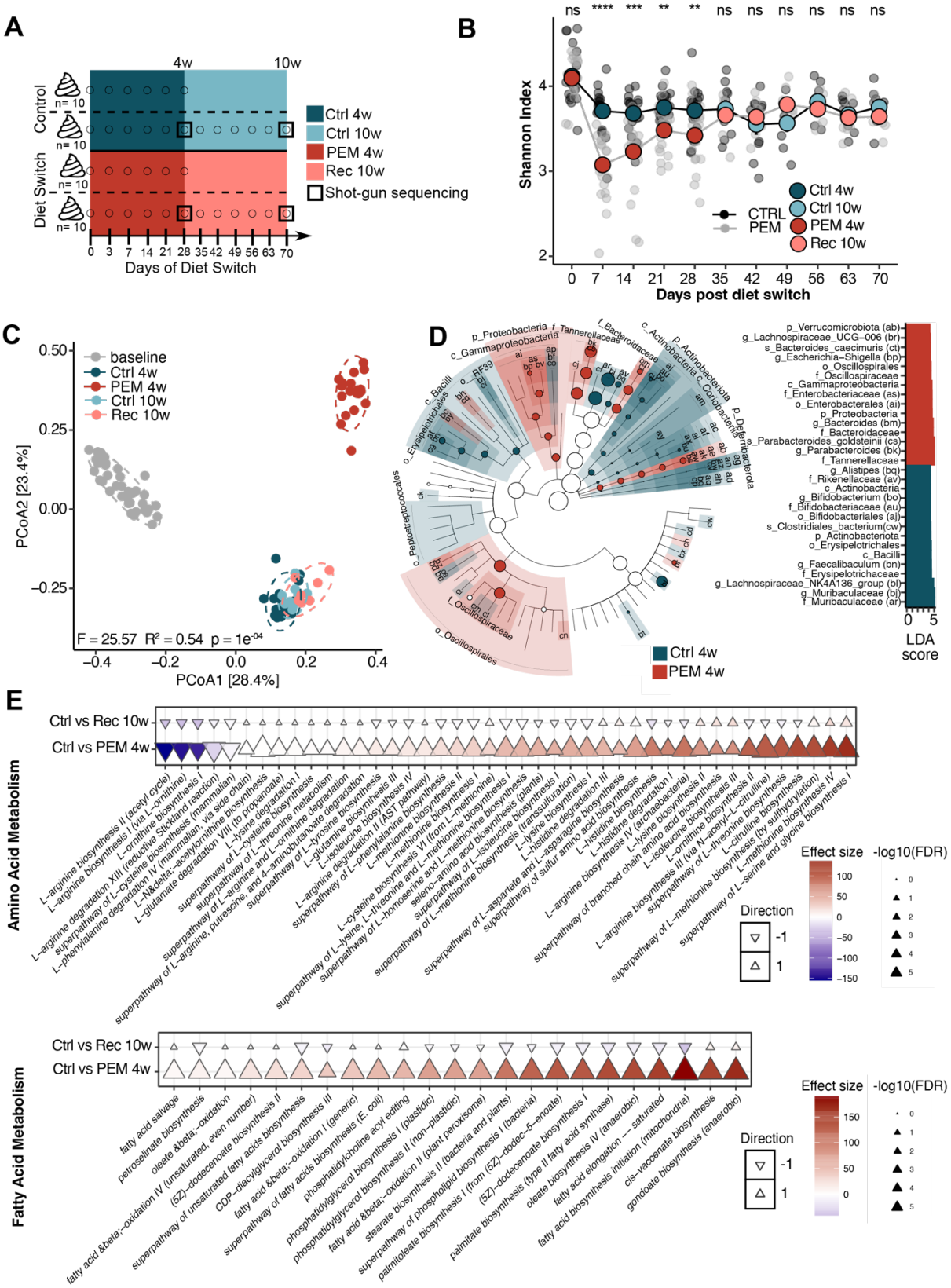

Figure 5: Acute PEM drastically alters microbiome composition and function. A) Stool sample collection scheme for microbiome analyses. Stool samples were collected weekly during the 10 weeks of diet experiment (normal or reduced protein diet) and used for 16S

1368 amplicon sequencing analysis and taxonomy characterization. Shot-gun metagenomic
1369 sequencing and functional potential analysis was performed only on stool samples from
1370 weeks 4 and 10 (Ctrl_4w, PEM_4w, Ctrl_10w and Rec_10w, each n=10 per group). **B)**
1371 Longitudinal alpha diversity of stool samples from mice under normal and reduced protein
1372 chow. Shannon index was computed at ASV level. Longitudinal cross-sectional comparisons
1373 were performed using Wilcoxon signed rank test. ns: not significant, *: $p < 0.05$, **: $p < 0.01$,
1374 ***: $p < 0.001$, ****: $p < 0.0001$. **C)** Principal Coordinate Analysis based on Bray-Curtis's
1375 distances of stool fecal microbiomes of mice during PEM and recovery to explore further
1376 differences in microbiome composition. Differences in the centroids of groups were tested
1377 with PERMANOVA with 10000 permutations. **D)** Linear discriminant analysis (LDA) effect size
1378 (Lefse) of the fecal microbiomes at peak acute PEM (day 28, PEM_4w versus Ctrl_4w). The
1379 cladogram depicts the phylogenetic distribution of differential taxa and the bar plot depicts
1380 differential taxa ranked by LDA. Differences are shown by the color of the most abundant
1381 class, with red indicating PEM_4w and blue indicating Ctrl_4w. The diameter of each circle
1382 corresponds to the abundance of the taxon. This analysis uses the SILVA v138 taxonomy. The
1383 bar plot represents the top 30 taxa based on LDA scores. The letters in brackets denote the
1384 abbreviation of the taxon shown in the cladogram. **E)** Differential amino acid and fatty acid
1385 metabolic microbiome pathways (PEM_4w vs Ctrl_4w and Rec_10w vs Ctrl_10w). The
1386 triangles show the hues and direction of the effect size (b coefficient). Color intensity and size
1387 represent the magnitude of the effect size and FDR significance of the specific pathway,
1388 respectively.

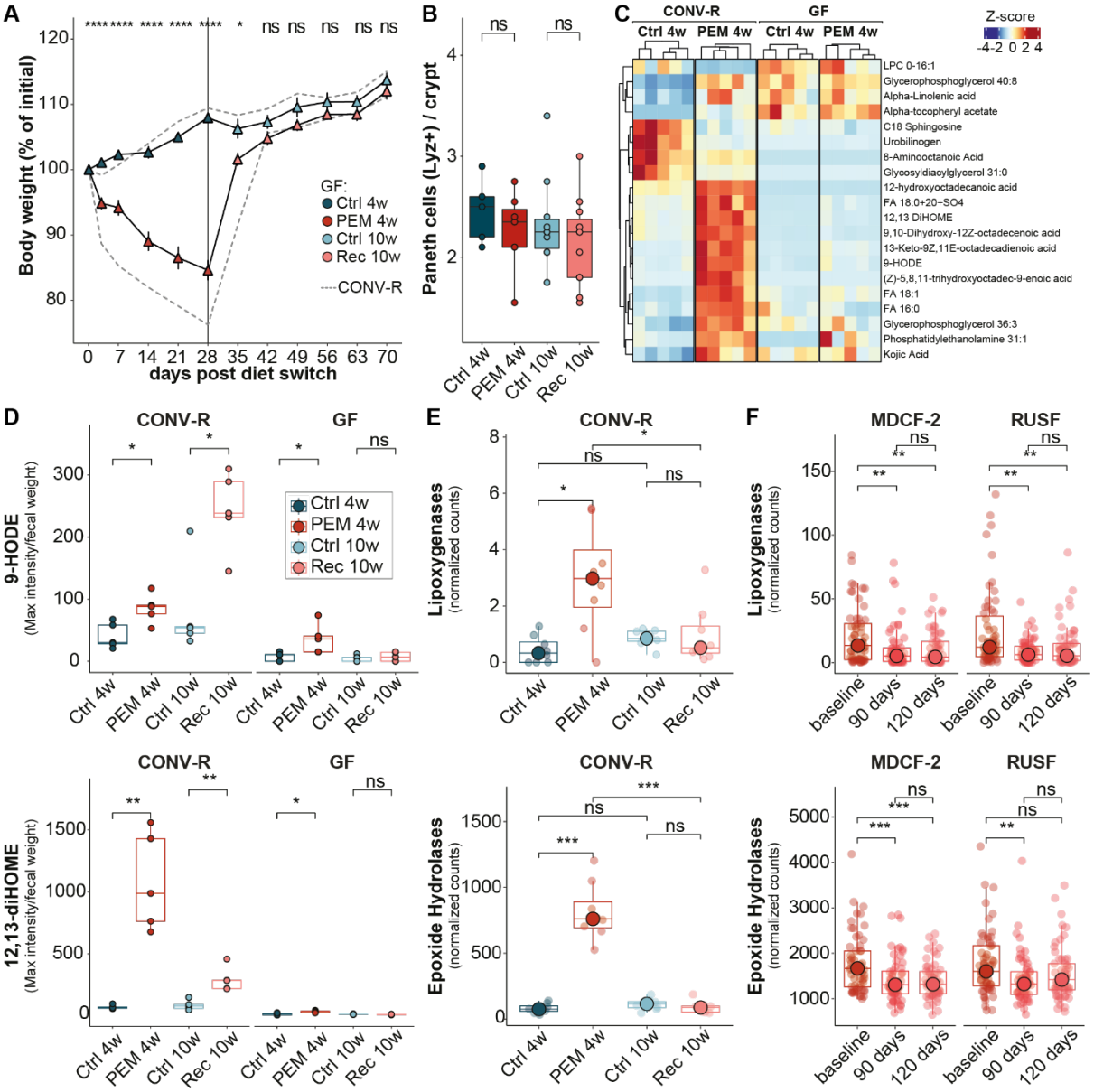

Figure 6: Absence of microbial signals attenuates the Paneth-cell phenotype and fecal metabolic alterations upon PEM. A) Body weight curves of GF mice without a microbiome under 4-week PEM regimen followed by 6-week recovery with regular diet compared to CONV-R mice with a regular microbiome. Note that GF mice displayed milder disease symptoms with significantly less body weight loss during PEM and a full recovery (n=10-11 mice per group). **B)** Paneth (LYZ1-positive) cell count in small intestinal sections of GF mice. **C)** Top 20 most significant lipid metabolites identified in feces of GF and CONV-R mice fed a CTRL or PEM for 28 days. **D)** Levels of 9-HODE and 12,13diHOME in feces of GF and CONV-R mice during the PEM & recovery experiment. **E)** Bacterial lipoxygenase and epoxide hydrolase (EH) genes identified in stool metagenomics of GF and CONV-R mice during PEM & recovery.

1400 **F)** Lipoxygenase and EH genes in feces collected on day 0, 90 and 120 of malnourished children
1401 undergoing a nutritional intervention with either a Microbiota Directed Complementary Food
1402 (MDCF-2) or standard Ready-to-Use Supplementary Food (RUSF) using published
1403 metagenomics data [10]. Data in (A) were compared by two-way ANOVA and in (B) and (D-F)
1404 using Wilcoxon signed rank test. ns: not significant, *: $p < 0.05$, **: $p < 0.01$, ***: $p < 0.001$,
1405 ****: $p < 0.0001$.

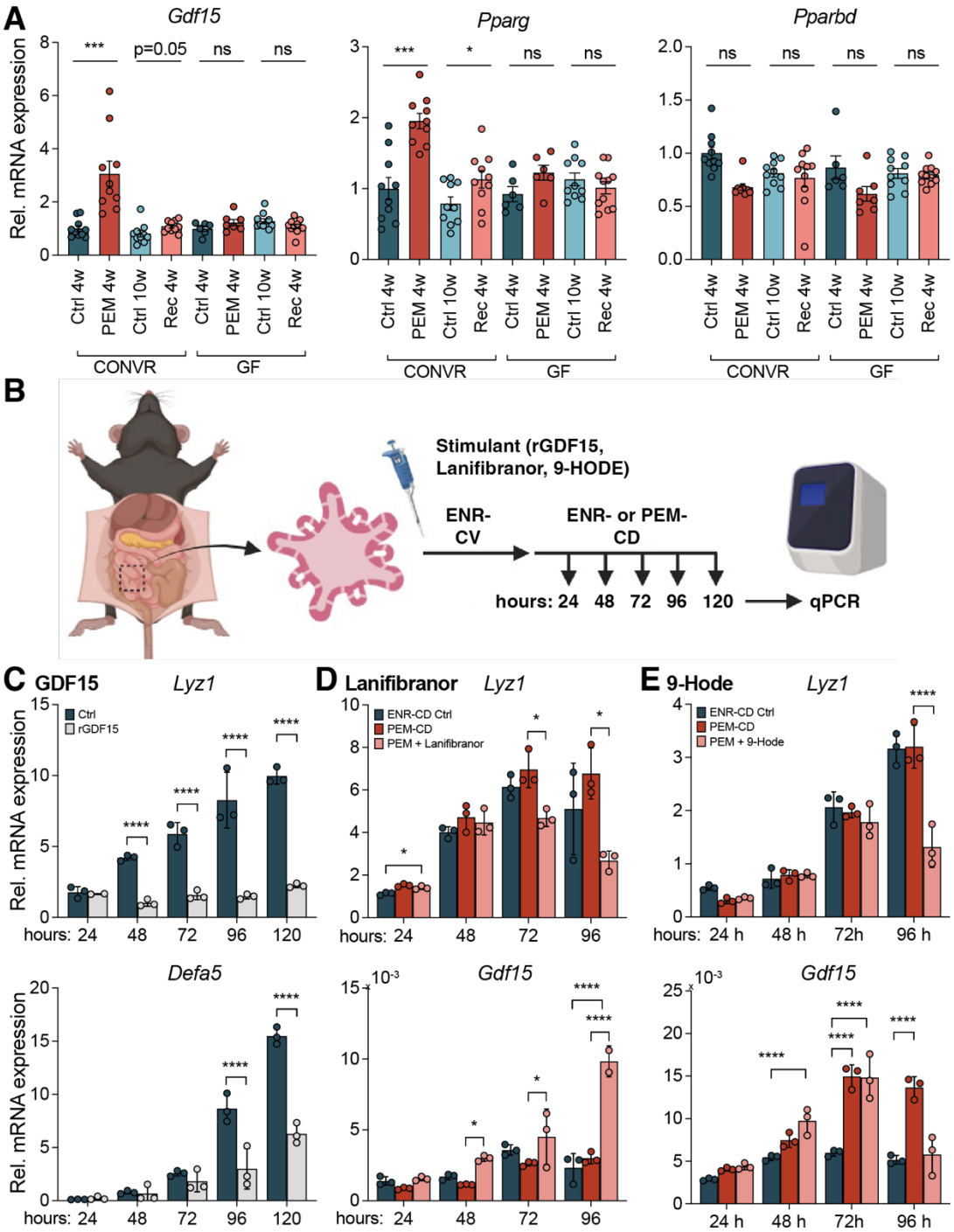

1406

1407 **Figure 7: Microbiome and PEM dependent factors block Paneth cell differentiation. A)**
1408 Expression of *Gdf15*, *Pparg* and *Pparbd* were assessed in small intestinal tissue of both CONVR
1409 and GF mice subjected to PEM and after recovery. *p < 0.05, ***p < 0.001 and ****p < 0.0001,
1410 ns = non-significant. Significance testing was performed using Wilcoxon-Mann-Whitney-Test.
1411 **B)** Schematic drawing of organoid intervention experiment. Murine intestinal organoids were
1412 first cultured in ENR-CV stem cell organoid medium and then Paneth cell differentiation was
1413 induced using ENR-CD or PEM-CD medium. Stimulants (recombinant GDF15 [1 µg/ml], pan-

1414 PPAR-agonist Lanifibranor [20 µM] or the lipid 9-HODE [1 µM] were added during initial ENR-
1415 CD and PEM-CD culture and kept throughout the experimental duration. All experiments were
1416 performed independently at least twice in triplicates. **C-E)** Relative *Lyz1*, *Defa5* and *Gdf15*
1417 mRNA expression in organoids during Paneth cell differentiation and stimulated with **(C)**
1418 recombinant GDF15, **(D)** the Pan-PPAR-agonist Lanifibranor or the lipid **(E)** 9-HODE. Note that
1419 PPAR-activation boosts GDF15 levels thereby blocking Paneth cell differentiation and the
1420 bacterial PEM metabolite 9-HODE also suppresses Paneth cell differentiation. *: $p < 0.05$, **:
1421 $p < 0.01$, ***: $p < 0.001$, ****: $p < 0.0001$ and ns = not significant using Mann-Whitney U test.

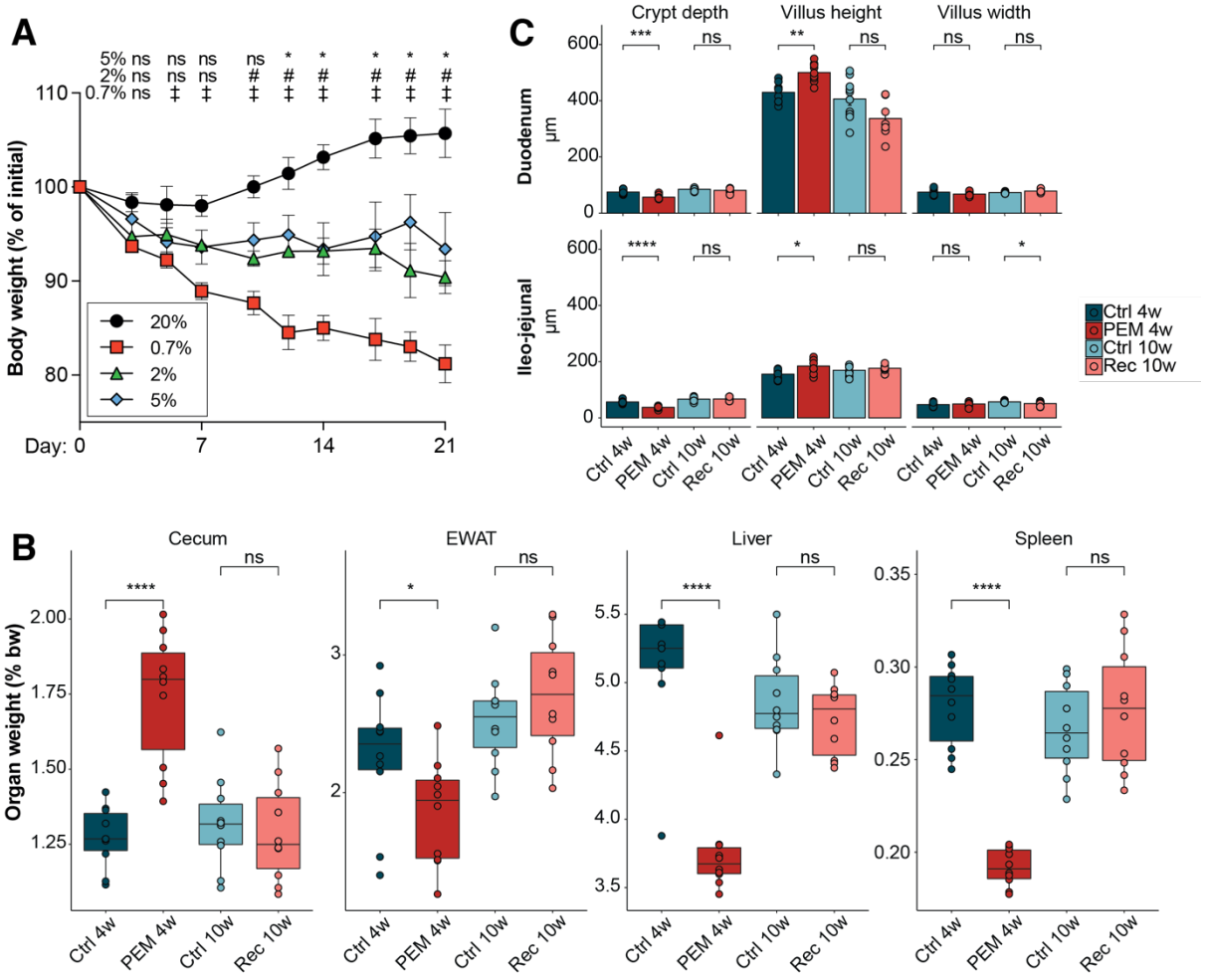

Figure S1: PEM drastically alters intestinal architecture and organ measures. A) Body weight development of adult mice fed either a control diet (20% protein) or PEM diets with various protein contents (0.7, 2 and 5%) for 3 weeks. **B)** Cecum, EWAT (epididymal white adipose tissue), liver and spleen weights relative to body weight of mice during the PEM diet and recovery intervention. **C)** Crypt depth, villus height and villus width from small intestine of mice during the PEM diet and recovery intervention.

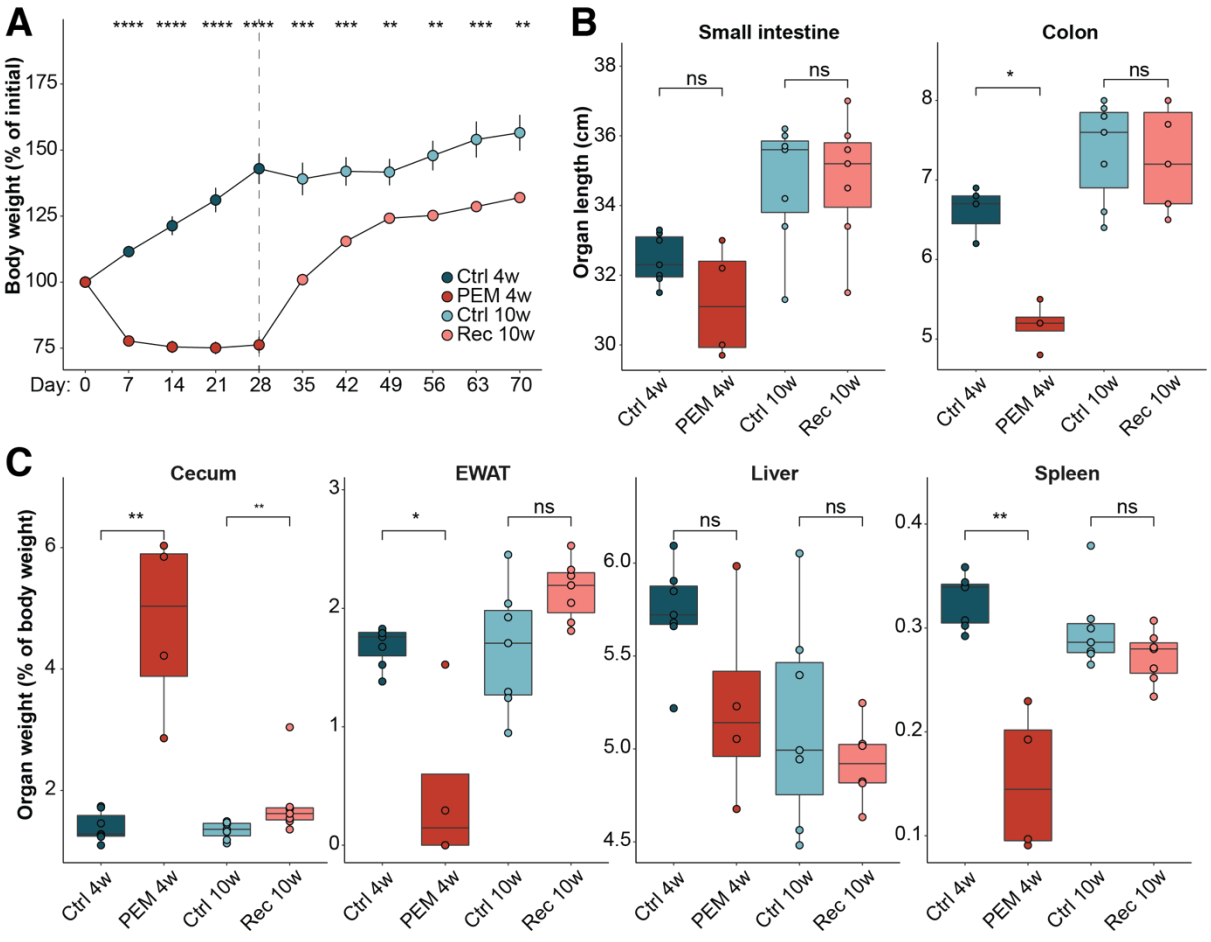

1429

1430 **Figure S2: PEM during postnatal development aggravates the disease phenotype. A)** Body
1431 weight curve of 4-week-old mice weaned onto PEM diet for 4 weeks and then switched to
1432 regular control diet for recovery. **p < 0.01, ***p < 0.001 and ****p < 0.0001 using two-way
1433 ANOVA. **B**) Lengths of the small and large intestine during PEM and recovery. *p < 0.05 and
1434 ns = not significant using Mann-Whitney U test. **C)** Cecum, EWAT (epididymal white adipose
1435 tissue), liver and spleen weights relative to body weight of mice during the PEM diet and
1436 recovery intervention. *p < 0.05, **p < 0.01 and ns = not significant using Mann-Whitney U
1437 test.

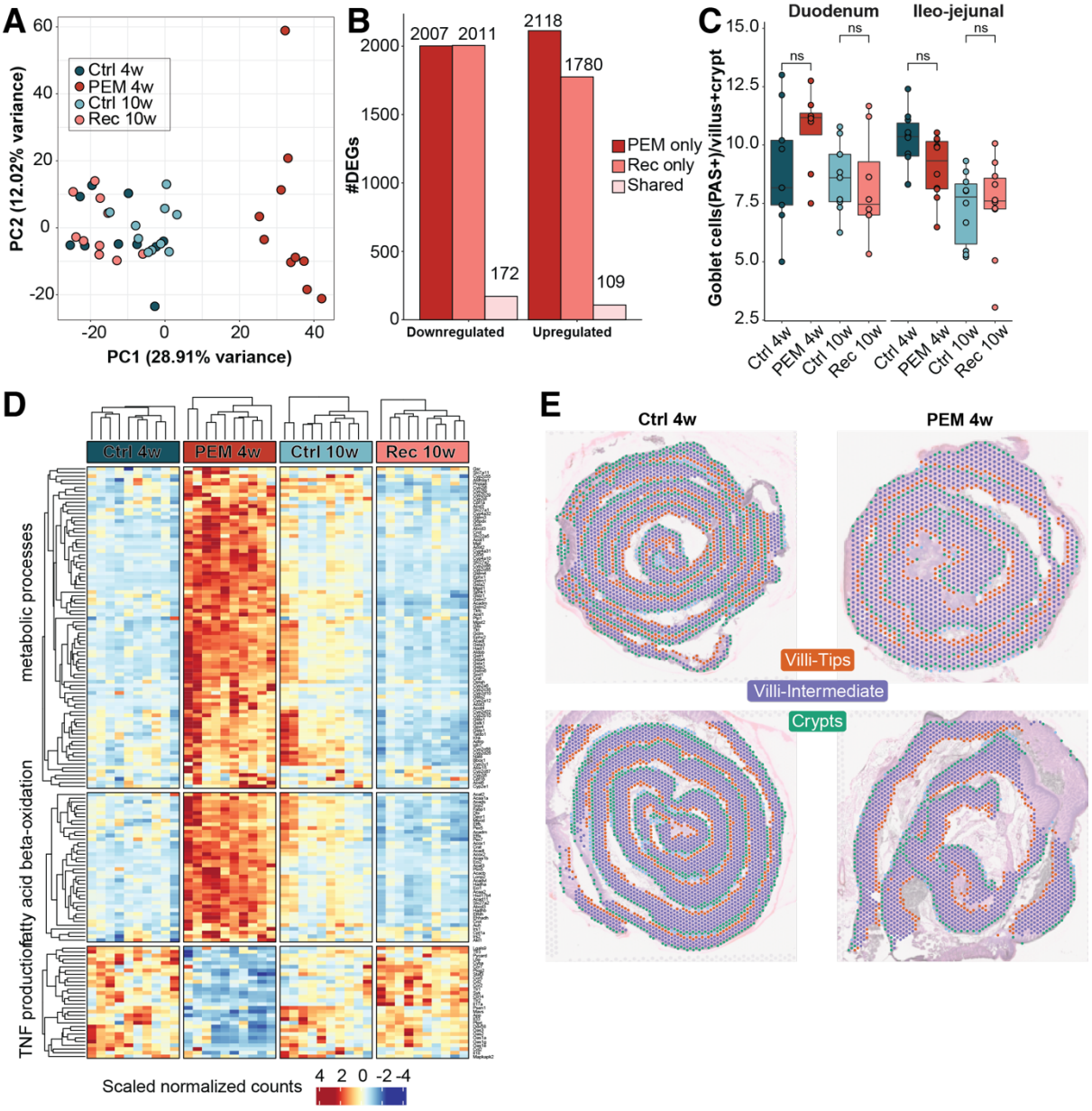

Figure S3: Differential regulation of genes in intestinal epithelial cells. A) Principal component analysis (PCA) for RNA sequencing samples. **B)** Number of significantly upregulated and downregulated genes in small intestinal epithelial cells from mice during acute PEM (4 weeks) and after recovery (10 weeks) and respective controls. **C)** Boxplots showing average number of goblet cells (PAS+) per villus and crypt in duodenum and ileo-jejunal regions of the small intestine of mice under Ctrl and PEM diets along with representative histological images. ns: $p > 0.05$ Ctrl_4w versus PEM_4w and Ctrl_10w versus Rec_10w using Mann-Whitney U test. **D)** Heatmap showing the expression of DEGs corresponding to selected GO terms enriched in upregulated and downregulated PEM only DEGs. Scaled normalized gene expression counts across all samples are plotted. **E)** Overlay of

spatial transcriptomic spots classified by different regions on high-quality H&E stainings from PEM_4w and Ctrl_4w mice.

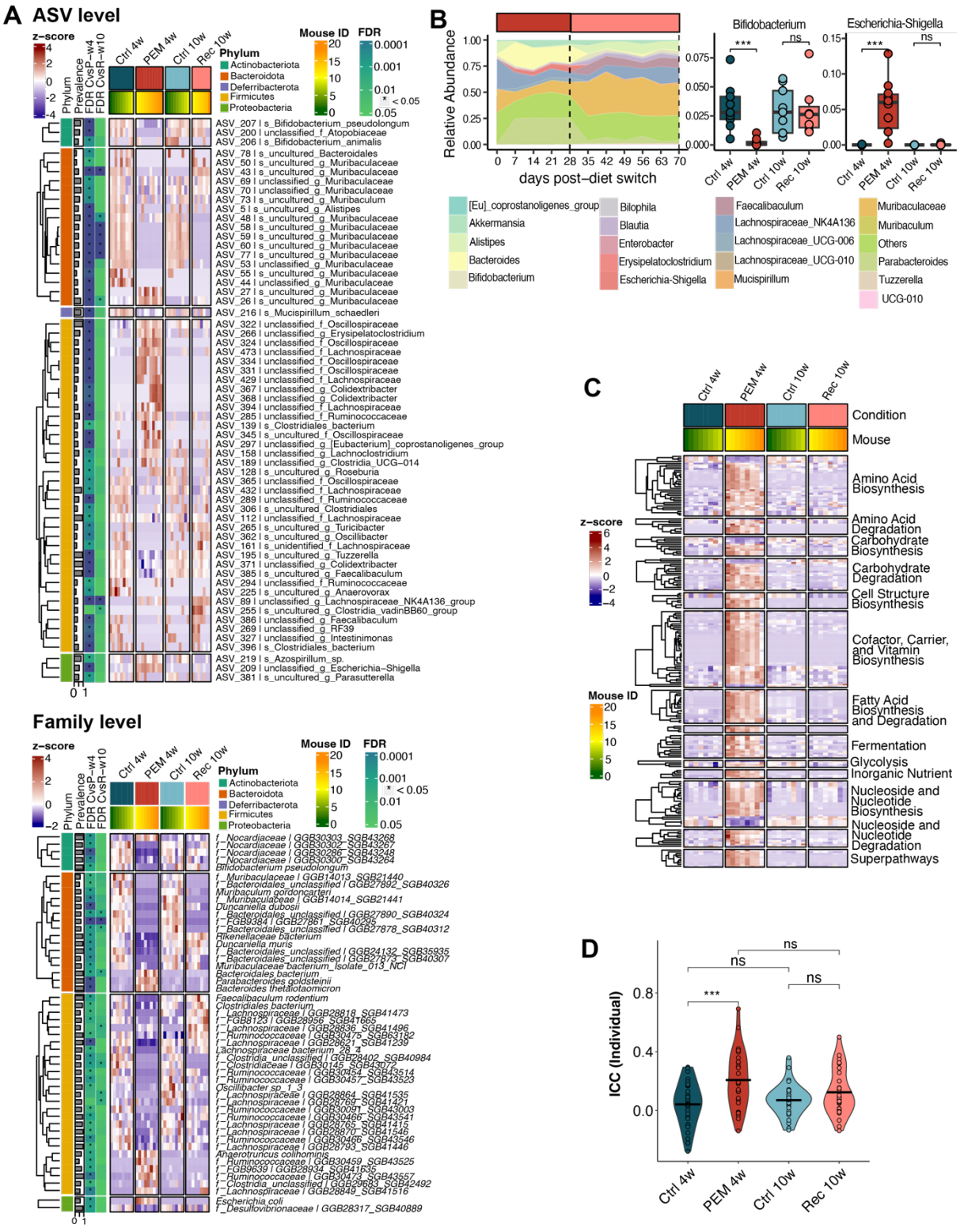

Figure S4: Longitudinal microbiome functions affected by PEM and recovery. A) Heatmap of relative abundance of bacterial species (ASV) and families with significant changes under acute PEM (PEM_4w vs Ctrl_4w) and after recovery (Rec_10w vs Ctrl_10w). For each cell, colors indicate the row-wise z-score of relative abundances, asterisks denote the FDR significance at each cross-sectional comparison and prevalence represents the percentage of

1457 non-zero features. Row-wise clusters represent features that belong to the same Phylum. **B)**
1458 Longitudinal area-stacked relative abundances of the top 20 significant genera identified by
1459 LefSe analysis. Unclassified genera and those with low relative abundance are grouped in
1460 "Others". Relative abundances comparisons of two representative genera, *Bifidobacterium*
1461 and *Escherichia-Shigella*. Wilcoxon signed rank test was used to test significance. **C)** Heatmap
1462 of abundances of microbiome metabolic pathways (obtained from HUMAnN 3.6) with
1463 significant changes under acute PEM (PEM_4w vs Ctrl_4w) and after recovery (Rec_10w vs
1464 Ctrl_10w). For each cell, colors indicate the row-wise z-score of relative abundances, asterisks
1465 denote the FDR significance at each cross-sectional comparison and prevalence represents
1466 the percentage of non-zero features. Row-wise clusters represent features that belong to the
1467 same higher-level pathway. **D)** Intraclass correlation coefficient (ICC) of individual genera
1468 across diet phases. Statistical differences were assessed by Wilcoxon signed-rank test.

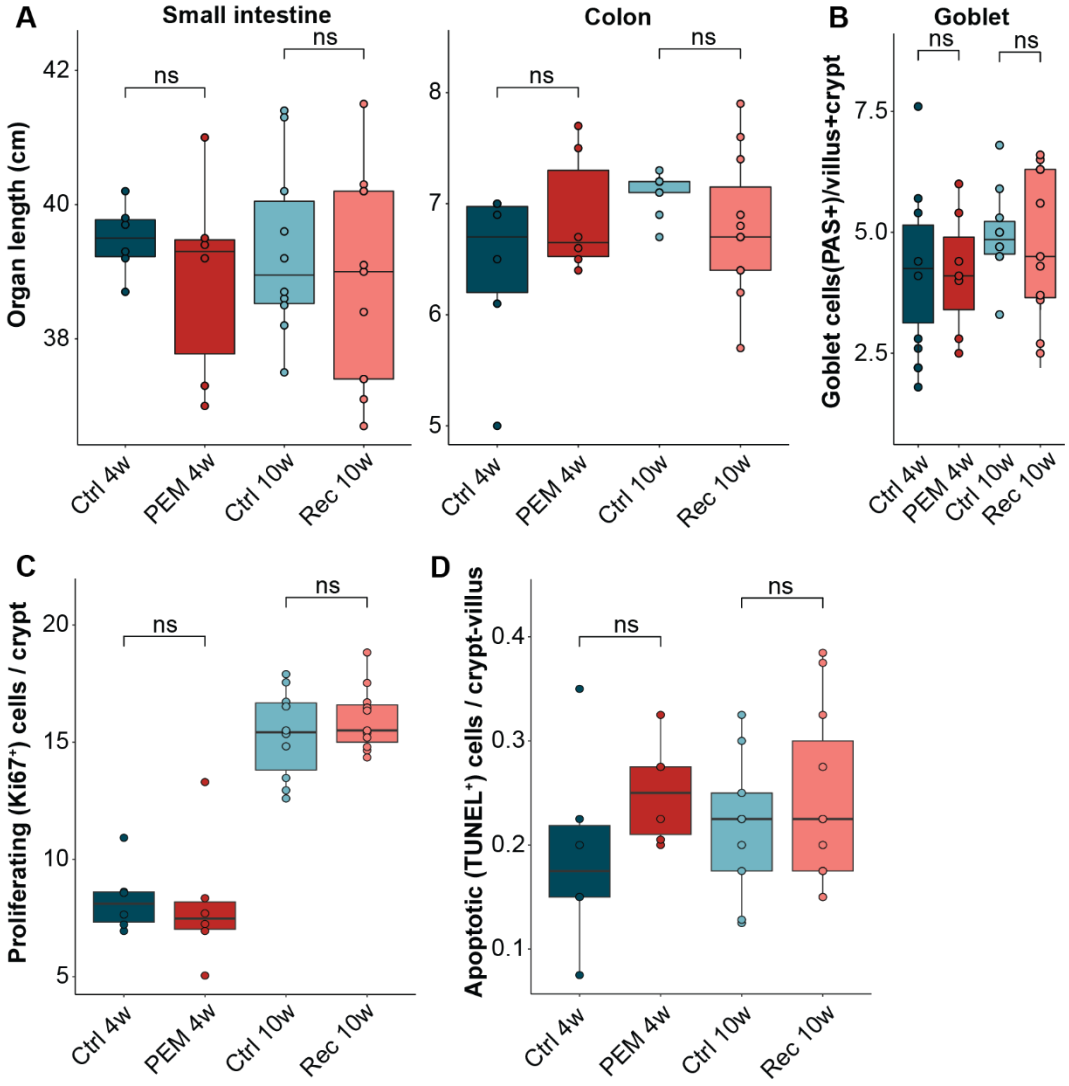

Figure S5: Ameliorated PEM phenotype in GF mice. GF mice (n=10-11 per group) were subjected to a dietary PEM-recovery intervention experiment and analyzed for organ measures and cell counts. **A)** Length of the small and large intestines. **B)** Number of PAS-positive goblet cells per villus-crypt-unit in intestinal small sections. **C)** Number of Ki67-positive proliferative epithelial cells per crypt. **D)** Number of TUNEL-positive apoptotic epithelial cells per crypt-villus unit. Significance testing was performed using Wilcoxon-Mann-Whitney-Test.

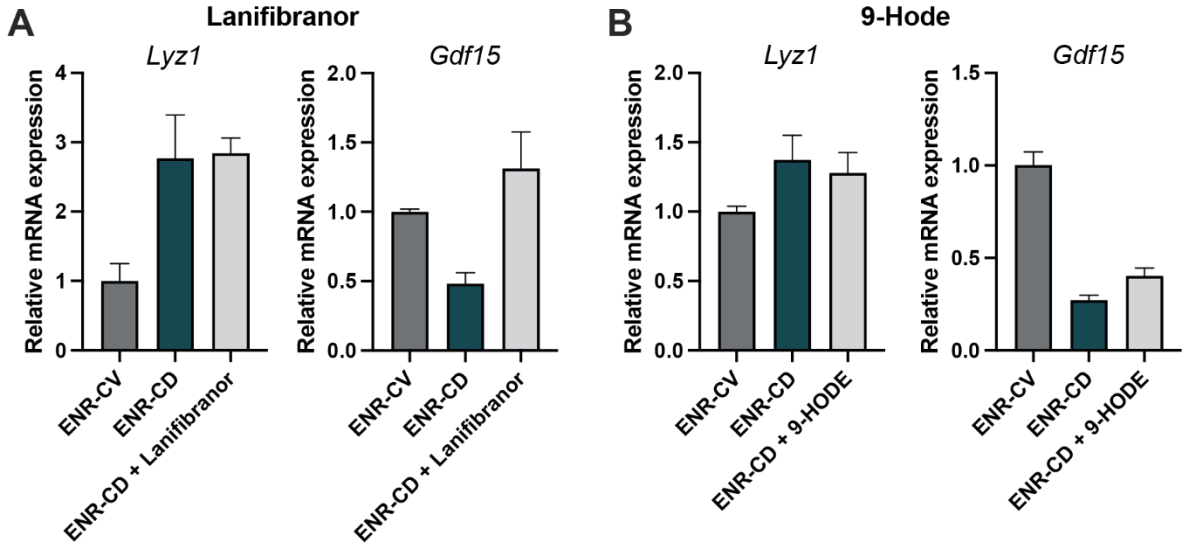

1477

1478 **Figure S6: PPAR-activation or the microbial metabolite 9-HODE alone do with Microbiome**
1479 **status and PEM drive *Ppar* / *Gdf15* expression and Paneth cell differentiation.** Expression of
1480 *Lyz1* and *Gdf15* were assessed in intestinal organoids stimulated with the **(A)** pan-PPAR-
1481 agonist Lanifibranor [20 µM] or the **(B)** lipid 9-HODE [1 µM] during Paneth cell differentiation.
1482 Note that stimulation with Lanifibranor or 9-HODE did not alter *Lyz1* or *Gdf15* expression in
1483 contrast to stimulation during PEM as shown in Figure 6.

1484 **Table S1: Formulation of PEM diets.**

Ingredient Product No. (Ssniff)	U	**0.7 % Protein** *S0071-E710*	**2.0 % Protein** *S0071-E711*	**5.0 % Protein** *S0071-E712*	**20.0 % Protein** *S0071-E714*
Casein	**%**	**0.680**	**2.200**	**5.600**	**21.500**
L-Cystine	%	0.100	0.100	0.100	0.300
Maltodextrin	%	32.020	30.500	27.100	11.000
Corn starch, pre-gelatinized	%	32.400	32.400	32.400	32.400
Dextrose	%	12.000	12.000	12.000	12.000
Sucrose	%	0.200	0.200	0.200	0.200
Cellulose powder	%	7.000	7.000	7.000	7.000
Inulin powder	%	2.300	2.300	2.300	2.300
Vitamin premix	%	1.000	1.000	1.000	1.000
Mineral premix AIN	%	5.000	5.000	5.000	5.000
Choline Cl (50 %)	%	0.250	0.250	0.250	0.250
Dye [Y, G, B, V, R]	%	0.050	0.050	0.050	0.050
Soybean oil	%	7.000	7.000	7.000	7.000
Proximate contents					
Crude protein	%	**0.7**	**2.0**	**5.0**	**19.0**
Crude fat	%	7.0	7.0	7.0	7.0
Crude fibre	%	8.4	8.4	8.4	8.4
Crude ash (minerals)	%	4.2	4.2	4.2	4.3
Carbohydrates	%	76.5	75.1	71.7	56.1
Energy (Atwater)	MJ/kg	15.6	15.6	15.6	15.5
kcal% Protein		0.7	2	5	21
kcal% Fat		17	17	17	17
kcal% Carbohydrates		82	81	78	62

1485

1486 **Table S2: List of** TaqMan® Gene Expression Assays **used in this study.**

Gene Name	**Gene Symbol**	**Assay**
Actin, beta	A*ctb*	Mm00607939_s1
Lysozyme 1	*Lyz1*	Mm00657323_m1
Defensin, alpha, 5	*Defa5*	Mm00651548_g1
Growth differentiation factor 15	*Gdf15*	Mm00442228_m1
Peroxisome proliferator-activated receptor gamma	*Pparg*	Mm01184322_m1
Peroxisome proliferator-activated receptor beta/delta	*Pparbd*	Mm00803184_m1

1487

1488 **Table S3: X500R MS parameters for non-targeted metabolomics and targeted identification**

1489 **of fatty acids (12,13-diHOME and 9-HODE)**

	Non-targeted metabolomics		**Targeted identification**	**Unit**
Method duration (minutes)	13.5	13.5	25	min
Total Scan Time	0.412	0.412	0.412	s
Curtain gas	30	30	30	psi
Ion source gas 1	45	45	45	psi
Temperature	500	500	500	°C
Ion source gas 2	45	45	45	psi
CAD gas	7	7	7	-
Polarity	**Positive**	**Negative**	**Negative**	-
Spray voltage	5500	-4500	-4500	V
TOF start mass	50	65	65	Dalton
TOF stop mass	1000	1000	1000	Dalton
Declustering potential	50	-50	-50	V
DP spread	0	0	0	V
Accumulation time	0.1	0.1	0.1	s
Collision energy	5	-5	-5	V
CE spread	0	0	0	V
IDA Criteria	Small molecule	Small molecule	Small molecule	-
Maximum candidate ions	10	10	10	-
Intensity threshold	1000	1000	1000	cps
TOF start mass	50	50	50	Dalton
TOF stop mass	1000	1000	1000	Dalton
Declustering potential	80	-80	-80	V
DP spread	0	0	0	V
Accumulation time	0.025	0.025	0.025	s
Collision energy	35	-35	-35	V
CE spread	15	15	15	V

1490